

ACTA POLYTECHNICA SCANDINAVICA

ELECTRICAL ENGINEERING SERIES No. 90

Thermal Analysis of High-speed Induction Machines

JUHA SAARI

Helsinki University of Technology
Laboratory of Electromechanics
P.O. Box. 3000, FIN-02015 HUT, Finland

Dissertation for the degree of Doctor of Technology to be presented with due permission for public examination and debate in Auditorium S1 at Helsinki University of Technology (Espoo, Finland) on the 30th of January, 1998, at 12 o'clock noon.

Saari J. **Thermal analysis of high-speed induction machines.** Acta Polytechnica Scandinavica. Electrical Engineering Series No. 90. Helsinki 1998. 73 p. Published by the Finnish Academy of Technology. ISBN 952-5148-43-2. ISSN 0001-6845. UDC 621.313

Keywords: Thermal analysis, friction loss, high-speed electric machine

ABSTRACT

A solid-rotor induction motor is suitable for rotation speeds 20 000-200 000 rpm in which the rotor surface speed exceeds 150 m/s. These machines need effective cooling because of their high power densities, and a proper model is needed for thermal analyses. The main aim of the research was to develop a thermal model for the solid-rotor induction machine. Another objective was to estimate the maximum power of the motor construction at different rotation speeds. Friction and gas-flow losses form a significant part of the total losses in high-speed electric machines. According to the measurement results presented in this thesis, these losses can be predicted by analytical equations. In addition, surface roughness caused by the stator slot openings does not significantly increase the friction losses in the air gap. A thermal-network model for the high-speed induction motor construction has been developed. The model is valid at different rotation speeds and cooling conditions of the machine. This results from the implementation of the friction and gas-flow losses, as well as from the convection heat-transfer coefficients to the model. The calculated temperature rises of the stator winding were within $\pm 10^{\circ}\text{C}$ the measured ones in the two high-speed motors tested. The thermal model was used to estimate the maximum power of the high-speed induction motor construction. For this reason, eight motors running at 50 000, 100 000, 150 000 and 200 000 rpm were analysed. The maximum power decreases with the rotation speed to the power of 2.1-2.2. The maximum power is obtained at the slip which gives the highest electrical efficiency of the machine. The power depends greatly on the coolant flow rate blown through the air gap. The utilisation factor and efficiency of the motor decreases when the rotor surface speed increases.

PREFACE

The research has been carried out during the years 1992-1997 as a part of a research project, "Development of a high-speed electric motor", in the Laboratory of Electromechanics, Helsinki University of Technology. The project has been financed by Technology Development Centre (TEKES) and High Speed Tech Ltd.

I would like to express my gratitude to Professor Tapani Jokinen for his guidance during the work. The basic construction of the high-speed electric motor was designed by Dr Antero Arkkio. In addition, he has made the electromagnetic optimisation of the motors presented in this thesis. I would like to thank him for all his help in my research work. I am obliged to Mrs Ruth Vilmi for revision of the language.

The measurements of friction losses in the air gap of a high-speed machine were carried out at Lappeenranta University of Technology. I would like to thank Mr Petri Sallinen for co-operation in the measurements. In addition, I would like to thank Associate Professor, Jaakko Larjola, for his advice concerning fluid mechanics and heat transfer.

Financial support by the Tekniikan Edistämissäätiö, Suomen Kulttuurirahasto (Hämeen rahasto) and Imatran Voima Foundation are gratefully acknowledged.

Espoo, 24 November 1997

Juha Saari

CONTENTS

ABSTRACT.....	2
PREFACE.....	3
CONTENTS.....	4
LIST OF SYMBOLS	5
1 INTRODUCTION	7
1.1 Development of a high-speed electric machine.....	7
1.2 Aim and scope of the research	8
2 ESTIMATION OF FRICTION AND GAS-FLOW LOSSES	9
2.1 Aim of the study.....	9
2.2 A literature review concerning the friction and gas-flow losses	9
2.3 Measurement of losses in the air gap	19
2.4 Comparison between measured and calculated results	25
2.5 Measurement of total friction losses	27
2.6 Discussion	29
3 THERMAL MODELLING OF HIGH-SPEED INDUCTION MACHINES	31
3.1 Aim of the study.....	31
3.2 Thermal-network model.....	32
3.3 Temperature-rise tests	37
3.4 Sensitivity of the model.....	41
3.5 Discussion	43
4 MAXIMUM POWER OF HIGH-SPEED INDUCTION MOTORS.....	45
4.1 Introduction	45
4.2 Construction of the high-speed motor	46
4.3 Thermal analysis of the high-speed motor	47
4.4 Maximum powers of high-speed induction motors.....	53
4.5 Discussion	55
5 CONCLUSIONS.....	57
REFERENCES	58
APPENDIX A: THERMAL NETWORK FOR HIGH-SPEED INDUCTION MACHINES	61
APPENDIX B: REFERRED HIGH-SPEED INDUCTION MACHINES IN FIGURE 17.....	70
APPENDIX C: PERFORMANCE OF THE HIGH-SPEED MOTORS	73

LIST OF SYMBOLS

C_f	Friction coefficient
C_p	Specific heat
G	Thermal conductance matrix
h	Heat transfer coefficient
J	Moment of inertia
k	Thermal conductivity
k_1	Roughness coefficient in the air gap
k_2	Velocity factor associated with the axial flow in the air gap
l	Length
n	Rotation speed
Nu	Nusselt number
p	Pressure
P	Power, power loss
Pr	Prandtl number
q_m	Mass flow rate
q_v	Volume flow rate
r	Radius
r_r	Radius of rotor
r_s	Inner radius of stator core
r_1	Inner radius of disk
r_2	Outer radius of disk
R	Gas constant
Re	Reynolds number
Re_a	Reynolds number of axial flow
Re_r	Tip Reynolds number of tangential flow
Re_δ	Couette Reynolds number of tangential flow
s	Axial clearance
t	Time
T	Torque
T	Temperature
ΔT	Temperature rise vector
Ta	Taylor number
u	Tangential velocity
u_r	Rotor surface speed
v	Axial velocity

δ	Radial air-gap length
ε_M	Eddy diffusivity of momentum
η_p	Polytropic efficiency of ventilator
μ	Dynamic viscosity
ν	Kinematic viscosity
ρ	Mass density
τ	Shear stress
τ_r	Shear stress on rotor surface
ω	Angular velocity

1 INTRODUCTION

1.1 Development of a high-speed electric machine

A novel electric motor construction has been developed at Laboratory of Electromechanics, Helsinki University of Technology (Patent U.S. 5473211, 1992). The motor has been designed to meet the following demands:

- Suitability for serial production
- Suitability for industrial use under normal operation conditions
- Rotation speed range 20 000-200 000 rpm
- Power range 30-500 kW
- Direct coupling between the electric motor and the load machine
- Frequency converter supply

Figure 1 presents a simplified drawing of the high-speed induction motor studied. The basic stator construction is similar to a normal 50 Hz motor. The rotor core is made of solid steel coated with a thin copper layer. The end-ring region has a thicker coating than the core region. The solid-steel construction enables the operation at rotor surface speeds to 550 m/s. A coated rotor together with end rings provides a better electric performance than a pure solid-steel rotor. Contactless bearings, such as magnetic and fluid bearings are used in the high-speed machine because conventional rolling bearings would have too high losses and too low a lifetime in the operation range considered. The high-speed machine has an open-circuit cooling in which the cooling gas is blown through the air gap and end-winding space.

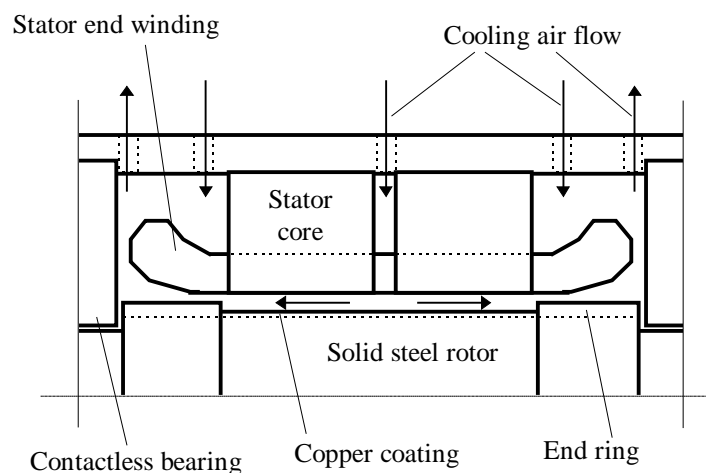


Figure 1. A schematic drawing of the high-speed induction motor developed at Helsinki University of Technology. Contactless operation of the rotor is provided by active magnetic or fluid bearings.

The new high-speed electric motor is mainly applied in turbomachines such as compressors or pumps. The turbomachine and the electric motor have a common shaft, and the rotation speed of the unit is controlled by a frequency converter. This means that the electric motor is operated at wide rotation speed and power ranges. A compressor may, for example, operate at powers from 40 to 140 kW and rotation speeds from 18 000 rpm to 30 000 rpm. In addition, the rotation speed and power changes a lot between different applications of high-speed machines. The electric motor for a refrigerator application may have ratings 2.5 kW and 200 000 rpm when the ratings maybe 300 kW and 18 000 rpm in a compressor application.

Effective calculation methods are needed in order to design high-efficiency motors for different high-speed applications. The electric losses and performance can be calculated rather accurately by using modern computation methods. On the other hand, the losses due to air friction and cooling are more difficult to calculate accurately. These losses form a large part of the total losses because they increase approximately to the cube of the rotation speed. The temperature rises in the stator winding and rotor sets the maximum power of the machine. The optimisation of the main dimensions and cooling of the electric machine requires a thermal model, in which the friction losses, convection heat transfer and cooling flow are properly modelled.

1.2 Aim and scope of the research

The aim of this research was to develop a thermal model for the high-speed induction machine and estimate the maximum power of the new motor construction.

Three independent research works are reported in this thesis. They are discussed in their own chapters. The first research (Chapter 2) deals with the calculation of the friction and gas-flow losses in high-speed machines. Chapter 3 presents a thermal-network model for the new high-speed induction machine construction. The maximum power of the motor construction is studied in Chapter 4. The last chapter summarises the conclusions and recommendations of the three research works.

2 ESTIMATION OF FRICTION AND GAS-FLOW LOSSES

2.1 Aim of the study

A large part of the total losses appear in the air space in a high-speed electric machine. This results from the high surface speed of the rotor which is typically above 150 m/s i.e. several times higher than in normal 50 Hz machines. In this work, the losses in air space are divided into friction losses and gas-flow losses. The friction losses are caused by the rotation of the rotor and they are proportional roughly to the cube of the rotor surface speed. The gas-flow losses are associated with the tangential acceleration of the coolant flow in the air gap. These losses are proportional to the product of the coolant flow rate and square of the rotor surface speed.

It is important to have rather accurate estimates for the friction and gas-flow losses. First, the efficiency of the machine depends greatly on these losses and they should be taken into account when designing the rotor main dimensions. Second, the losses are needed in the cooling design (coolant flow rate, coolant flow paths) of the machine.

The aim of the study was to investigate if one can calculate the friction and gas-flow losses of a high-speed machine by analytical equations. A special attention was paid on the effect of the surface roughness in the air gap caused by the stator slots.

2.2 A literature review concerning the friction and gas-flow losses

Friction torque of rotating cylinder and disk

Friction losses are set by the velocity field and gas properties. The velocity distribution in the air gap of electric machines is controlled by the following flows:

- Tangential flow due the rotor rotation
- Axial flow of the cooling gas through the air gap
- Taylor vortices due to centrifugal forces.

The importance of each flow depends on the peripheral speed of the rotor, flow rate and physical properties of the coolant as well as air-gap dimensions.

The nature of a gas flow is determined by the ratio between the inertia and viscous forces, called the Reynolds number (Reynolds 1974). The tangential flow is forced by the rotating rotor and the turbulence is described by the Couette Reynolds number

$$Re_{\delta} = \frac{\rho u_1 \delta}{\mu} \quad (1)$$

where ρ is the density and μ is the dynamic viscosity of the fluid, u_1 is the peripheral speed of the rotor and δ is the air-gap length in radial direction. When a cylinder is rotating in free space i.e. without a stator, the Reynolds number is called as the tip Reynolds number and it has the form

$$Re_r = \frac{\rho u_1 r}{\mu} \quad (2)$$

where r is the radius of the cylinder. Equation 2 can also be used to calculate the Reynolds number for a rotating disk. For an axial flow through the air gap the Reynolds number is

$$Re_a = \frac{\rho v_m 2\delta}{\mu} \quad (3)$$

where v_m is the mean axial fluid velocity. It is calculated by the volume flow rate and the cross-section of the air gap.

When the Reynolds number is below 2000, all the fluid particles are flowing in the same direction and the flow is laminar. If we increase the fluid velocity, the Reynolds number increases and velocity fluctuations appear in the flow. All the fluid particles are no longer moving to the same direction, although one mean direction can be determined. This kind of a flow is turbulent and it appears at lower velocities if there is surface roughness or curves in the flow channel. The gas flow inside a high-speed electric motor is usually turbulent.

Figure 2 presents the tangential and axial velocity distributions of the air-gap flow. The tangential flow is viewed from the end of the machine and the curvature of the air gap is neglected. The fluid velocity near the rotor is the same as the surface speed of the rotor. Correspondingly, the velocity near the stator is zero. For the laminar flow, the velocity distribution is linear. In the turbulent case, one can separate three layers: Two viscous layers near the walls and one fully turbulent layer in the middle flow. In the viscous layers, the generation of friction, as well as energy transfer, is determined mainly by the molecular viscosity of the fluid. The thickness of the layer decreases with an increasing Reynolds number. In the middle flow, the chaotic motion of fluid particles is independent of viscosity. The highest velocity gradients in the mean velocity are in the viscous layers. The lower figures show side views of axial air-gap flows. In the laminar flow, the fluid velocity has a parabolic distribution. In the turbulent flow, one can separate the same regions as in the tangential flow. In addition to Reynolds number, the velocity distribution is affected by the roughness on the wall surface. In general, roughness decreases the velocity gradients in the flow.

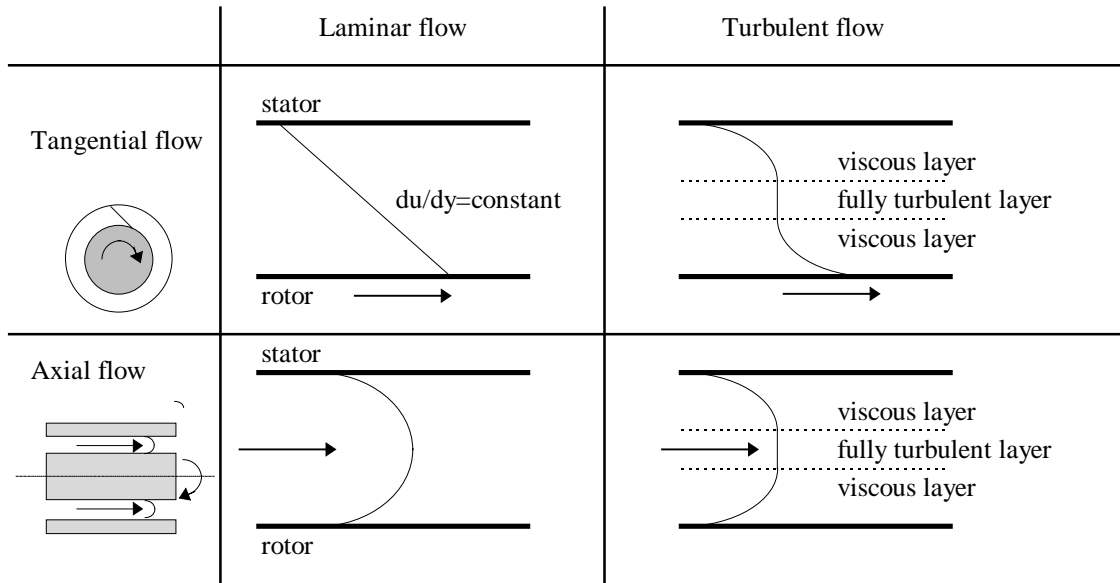


Figure 2. Tangential and axial velocity profiles of laminar and turbulent air-gap flows.

The calculation of fluid velocities is based on Navier-Stokes and continuity equations. These equations can be solved analytically in the case of a laminar flow and a simple geometry. Turbulent flows, however, are more difficult to analyse, because the viscosity terms in the equations have to be replaced by terms for turbulent frictional stresses. These parameters are semi-empirical constants. If turbulent flows are analysed analytically, the flow is usually divided into several layers and each layer is analysed separately. Turbulent flows in engineering have been discussed, for example, by Reynolds (1974).

Taylor vortices are circular velocity fluctuations appearing in the air gap (Fig. 3a). They are due to the centrifugal force affecting the fluid particles. At low rotation speeds the flow is laminar, because the creation of vortices is damped by frictional forces. In addition to the Couette Reynolds number, the creation depends on the air-gap length. These parameters are included into the Taylor number

$$Ta = Re_{\delta}^2 \frac{\delta}{r_1} = \frac{\rho^2 \omega^2 r_1 \delta^3}{\mu^2} \quad (4)$$

where ω is the angular velocity. The rotor radius should be replaced with the mean air-gap radius if the air-gap length is large. In a simple rotor-stator system, Taylor vortices occur when the Taylor number exceeds 1.7×10^3 (Gazley 1958). This figure is called the critical Taylor number.

The critical Taylor number is affected by many aspects, such as the ratio between the rotor and stator radii, temperature of the rotor and stator, as well as the flow rate of the cooling fluid. The effect of the axial flow is very significant. Four flow regimes have been separated according to Taylor vortices and turbulence of the axial flow. These regimes are shown in Fig. 3b. The figure, however, does not show the disappearance of the Taylor vortices which is supposed to happen

above $Re_\delta=5 \times 10^4$ (Smith and Townsend 1982). A comprehensive review, dealing with the Taylor vortices between concentric cylinders, have been reported by Di Prima and Swinney (1981).

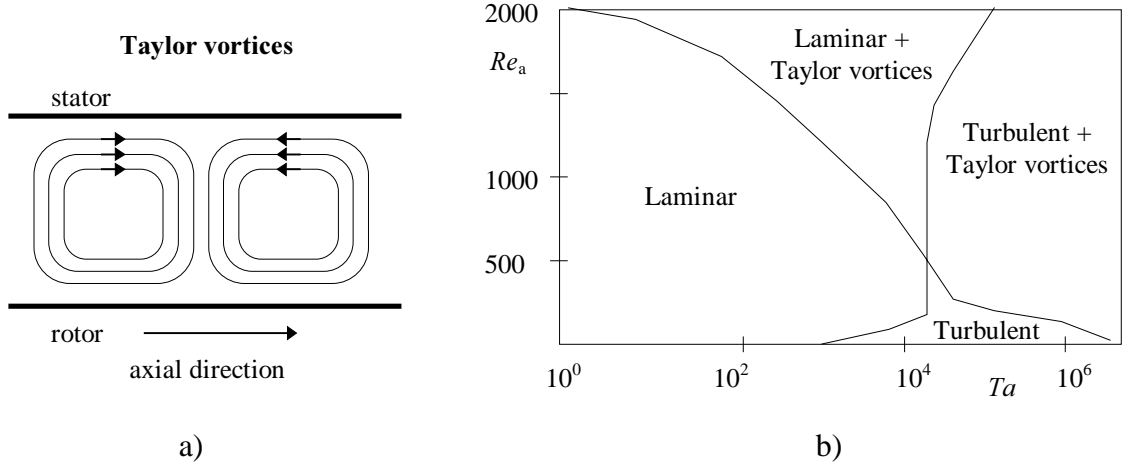


Figure 3. a) Side view of the Taylor vortices in the air gap. b) Flow regimes for superimposed tangential and axial flows in the air gap (Dorfman 1963).

The tangential force per area is described as a shear stress. If we consider a laminar flow between two concentric cylinders, the shear stress has the equation

$$\tau = \rho \nu r \frac{\partial}{\partial r} \left(\frac{u}{r} \right) \quad (5)$$

where ν is the molecular viscosity, r is the radius and u is the tangential fluid velocity. In fully turbulent flows, the shear stress is set by the chaotic motion of fluid particles, and the fluid viscosity is a minor factor. The shear stress for turbulent flows is written into the form

$$\tau = \rho (\nu + \varepsilon_M) r \frac{\partial}{\partial r} \left(\frac{u}{r} \right) \quad (6)$$

where ε_M is the eddy diffusivity of momentum. It increases when the distance from the wall increases. In order to calculate Eq. 6, one should know the velocity distribution and eddy diffusivity in the flow. There are no complete models for turbulence and these factors, therefore, are based on measured data.

The shear stresses near the walls are the ratio between the forces and surface areas. In the axial direction, the frictional forces are balanced by pressure forces in the air gap. The force needed to move the fluid through the air gap is maintained by a ventilator. In the tangential direction, the frictional forces are balanced by the electromagnetic torque acting on the rotor. This report focuses on the friction torque, pressure forces are not discussed.

As the shear stresses in turbulent flows are difficult to solve, the frictional drag is usually defined by a dimensionless friction coefficient. It is an empirical coefficient depending on many factors, such as the nature of the flow and the surface quality. For a rotating cylinder, the friction coefficient is

$$C_f = \frac{\tau_1}{\frac{1}{2}\rho u_1^2} \quad (7)$$

where τ_1 is the shear stress on the rotor surface. By using Eq. 7 and the definition of the torque, one can write

$$T = C_f \rho \pi \omega^2 r_1^4 l \quad (8)$$

where l is the axial air-gap length. Equation 8 gives the friction torque acting on the rotor. For a rotating disk, the friction torque is calculated with the equation

$$T = \frac{1}{2} C_f \rho \omega^2 (r_2^5 - r_1^5) \quad (9)$$

where r_1 and r_2 are the inner and outer radii of the disk, respectively.

Friction coefficient of rotating cylinder

A historical review concerning friction coefficients of rotating cylinders is given in the following pages. One paper deals with rotating cylinders in free space and the rest with concentric cylinders. The papers are discussed in chronological order. The cylinders and flow ranges used in the measurements are presented at the end of the review (Table 1).

One of the earliest studies dealing with the friction torque of rotating cylinders was published by Wendt (1933). Three different cylinders were tested at Couette Reynolds numbers up to 10^5 . Pure water and water-glycerol mixtures were used in the experiments. His measured data fit well with the following equations

$$C_f = \frac{0.46 \left(\frac{(r_2 - r_1)r_2}{r_1^2} \right)^{0.25}}{Re_\delta^{0.5}} \quad (400 < Re_\delta < 10^4) \quad (10a)$$

$$C_f = \frac{0.073 \left(\frac{(r_2 - r_1)r_2}{r_1^2} \right)^{0.25}}{Re_\delta^{0.3}} \quad (10^4 < Re_\delta < 10^5) \quad (10b)$$

where r_2 is the inner radius of the outer cylinder.

Theodorsen and Regier (1944) have made a detailed study of friction torque of rotating cylinders in free space. The tests were carried out in air, oil, kerosene and water and the highest tip Reynolds number achieved was 4×10^5 . Both smooth and rough cylinders were used in the measurements. At a Reynolds number of 10^5 , the friction coefficient increased from 6.3×10^{-3} to 15.8×10^{-3} , when the cylinder surface was roughened with grains of sand. The size of the particles was 3% of the cylinder radius. The friction-coefficient curves of rough cylinders deviated from the curve of the smooth cylinder at lower Reynolds numbers when the particle size was increased. The deviation occurred, when the viscosity layer was decreased below the particle size. Above the critical point the friction coefficient was independent of Reynolds number. Theodorsen and Regier measured rotating disks with supersonic speeds and found that the friction coefficient does not depend on the Mach number.

Yamada (1962a) measured the friction torque between concentric cylinders with the inner cylinder rotating. He used smooth and circumferentially grooved cylinders in his experiments. In addition to the tangential flow, he had also an axial flow through the air gap. The tests were carried out in water and spindle oil, and the highest Couette and axial Reynolds numbers obtained were 6×10^4 and 2×10^4 , respectively. The torque was measured in the test section where the velocity field was assumed to be fully developed. By neglecting the curvature of the air-gap surfaces and the occurrence of Taylor vortices, Yamada developed an equation for the friction coefficient

$$\frac{1}{\sqrt{2C_f}} = 7.54 + 11.5 \log_{10} \left(Re_{\delta} \sqrt{2C_f} \right) \quad (11)$$

Equation 11 gave lower friction coefficients than the measurements. The difference increased with an increasing radial air-gap length. This was due to the Taylor vortices, which appear at lower Couette Reynolds number when the air-gap length is increased. Equation 11 can be written into a more practical form

$$C_f = \frac{0.0152}{Re_{\delta}^{0.24}} \quad (800 < Re_{\delta} < 6 \times 10^4) \quad (12)$$

Yamada assumed that the fluid velocity varies proportionally to the distance from the air-gap midpoint with the power of $1/7$. When the fluid has both tangential and axial velocity components, the friction coefficient is

$$C_f = \frac{0.0152}{Re_{\delta}^{0.24}} \left[1 + \left(\frac{8}{7} \right)^2 \left(\frac{4Re_a}{Re_{\delta}} \right)^2 \right]^{0.38} \quad (13)$$

Under an axial Reynolds number of 2×10^3 , the friction coefficient decreased with an increased axial Reynolds number. Above $Re_a = 2 \times 10^3$, the friction coefficient increased with an increased axial flow.

Above a Couette Reynolds number of 3×10^4 , the friction coefficient was independent of the axial Reynolds number. This was tested up to $Re_a = 10^4$. These variations were due to the stabilising effect of the axial flow (see Fig. 3b). Equation 13 does not model these effects. The friction coefficients for circumferentially grooved rotors were mainly lower than for smooth rotors. The effect of grooves, however, decreased at high Couette Reynolds numbers ($> 10^4$).

Bilgen and Boulos (1973) have measured friction torque of enclosed smooth cylinders having Couette Reynolds numbers between 2×10^4 and 2×10^6 . Based on their own measurements and the experiments by some other authors, they developed equations for the friction coefficient. In the turbulent region, the friction coefficients are

$$C_f = 0.515 \frac{\left(\frac{\delta}{r_1}\right)^{0.3}}{Re_\delta^{0.5}} \quad (500 < Re_\delta < 10^4) \quad (14a)$$

$$C_f = 0.0325 \frac{\left(\frac{\delta}{r_1}\right)^{0.3}}{Re_\delta^{0.2}} \quad (10^4 < Re_\delta) \quad (14b)$$

The experimental friction coefficients deviated less than 8.35% from the results calculated by Eqs. 14. The ratio of the air-gap length to the rotor radius is included into the equation to model the effect of the Taylor vortices. Two more equations were fit with results for flows in the laminar and transition regimes.

Polkowski (1984) has applied the general solution of momentum equation (Dorfman 1963) into rotor-stator systems when there is an axial flow in the air gap. He compared the friction coefficient with those calculated for Couette flows neglecting the curvature of the air gap (r_1 and $r_2 \rightarrow$ infinity). The assumption of a Couette flow in the air gap led to lower friction coefficients than the use of the momentum equation. The difference grew when the ratio between the air-gap length and rotor radius was increased. In his paper, Polkowski underlined that a rather large friction torque may be associated with the entrance effects of the axial air-gap flow. He suggested that the torque needed to accelerate the axial cooling gas into a tangential movement follows the equation

$$T = \frac{2}{3} \pi \rho (r_2^3 - r_1^3) v_m u_m \quad (15)$$

where v_m and u_m are the mean axial and tangential fluid velocities, respectively. Equation 15 assumes that the cooling fluid has only an axial velocity component before entering the air gap. The mean tangential velocity is usually expected to be half of the surface speed of the rotor. In addition, Polkowski derived the axial air-gap length in which the acceleration takes place. This length is increased by the flow rate of the cooling gas and decreased by the rotation speed.

Ueyama and Fujimoto (1990) have measured friction losses of different kinds of rotors. The rotors were levitated with active magnetic bearings. The separation between iron and friction losses was made by carrying out deceleration tests both in air and vacuum. The measured data agreed well with Eq. 12 presented by Yamada.

Very accurate torque and wall shear stress measurements, as well as flow visualisation of rotating cylinders, have been reported by Lathrop et al. (1992a and 1992b). They operated at Couette Reynolds numbers from 800 to 1.23×10^6 , and different water-glycerol mixtures were used as the working fluid. The measured friction torques were in agreement with Eq. 10 (Wendt 1933) within $\pm 15\%$. A careful analysis, however, showed that the Reynolds-number dependency of the torque is not constant but increases from 1.23 to 1.87 at $3 \times 10^3 < Re_\delta < 10^6$. Above the transition to a fully irregular turbulent flow ($Re_\delta > 1.3 \times 10^4$), Lathrop et al. were able to predict the torque in the same way as for open-wall bounded shear flows (pipe flow, duct flow etc.).

The discussion of scaling laws for the angular momentum of a completely turbulent Couette flow has been continued by Panton (1992). He presented a theory similar to that for channel flow, except that the angular momentum was replaced by the velocity. Thin wall layers and an inviscid core region were assumed in the analysis. The theory is applicable at high Couette Reynolds numbers ($> 10^4$) when the Taylor vortices have disappeared.

Table 1. Test conditions used in the friction torque measurements.

Author	Fluid	Rotation speed [rpm]	Rotor dimensions r, l, δ [mm]	Reynolds number Re_δ, Re_a, Re_r	Surface quality
Wendt (1933)	water water-glycerine	–	100.0–137.5 580 9.5–47.0	– – –	smooth
Theodorsen and Regier (1944)	air, oil kerosene water	–	152.4–1219.2 6.4–76.2 free cylinder	– – $4-4 \times 10^5$	smooth, roughness in rotor
Yamada (1962a)	water spindle oil	$90-5 \times 10^3$	180 28.8–31.7 0.43–3.32	$6 \times 10^3-6 \times 10^4$ $0-2 \times 10^4$ –	smooth, circumferential grooves in rotor
Bilgen and Boulos (1973)	water water-glycerine	$300-1.5 \times 10^3$	212.7–249.2 127 0.31–1.75	$2 \times 10^4-6 \times 10^4$ – –	smooth
Ueyama and Fujimoto (1990)	air	$0-10^5$	13.8 – –	– – –	smooth
Lathrop et al. (1992a and b)	water- glycerine	0–900	160.0 695.0 60.85	$800-1.2 \times 10^6$ – –	smooth

Friction coefficient of rotating disk

The friction coefficient in Eq. 9 depends on the Reynolds number and dimensions of the enclosure: when the dimensions and the Reynolds number are in certain regimes, the rotating disk is operating as a centrifugal pump. This is illustrated in Fig. 4a.

A very detailed study, dealing with smooth, rotating disks in enclosures has been published by Daily and Nece (1960). Their experiments cover the Reynolds numbers from 10^3 to 10^7 and spacing ratios from 0.0127 to 0.217. The spacing ratio is described in Fig. 4. In addition to the torque measurements, they studied the tangential and radial velocity distribution as well as pressures in enclosures. According to the turbulence and occurrence of the pumping effect, Daily and Nece separated four different flow regimes for a rotating disk. These regimes are presented in Fig. 4b.

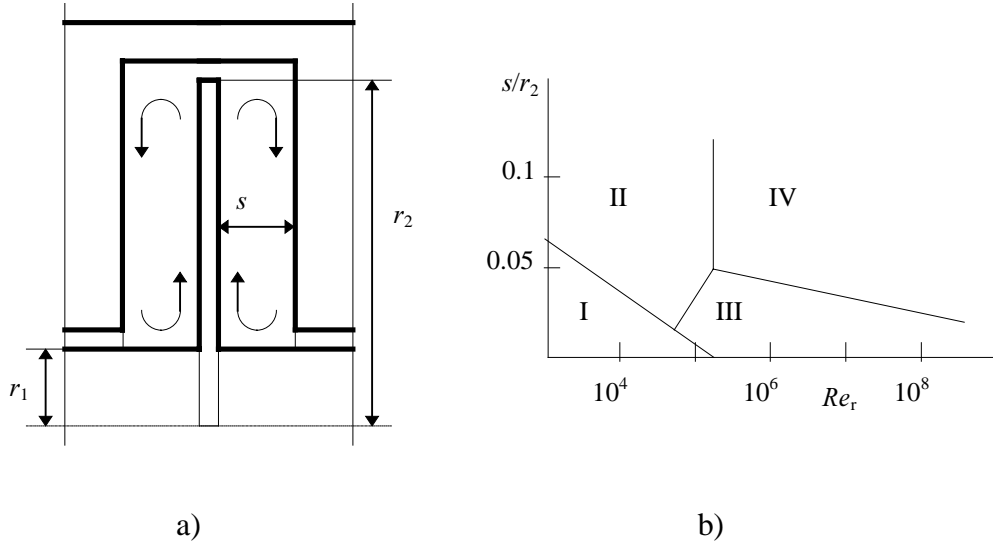


Figure 4. a) Rotating disk in an enclosure. The disk acts like a centrifugal pump: fluid flows radially outward near the rotating disk, axially across the clearance and radially inward on the stationary wall. When the axial clearance is decreased, the boundary layers of the disk and wall merge, and only a tangential velocity component is left. The ratio s/r_2 is called the spacing ratio. b) The approximate flow regimes for enclosed rotating disks (Daily and Nece 1960). Regimes I and II represent laminar and III and IV turbulent flows. The radial pumping effect exists in regimes II and IV. The flows in Regimes I and III have only the tangential velocity component.

The friction coefficients for the different flow regimes shown in Fig. 4b have the equations

$$C_f = \frac{2\pi}{\left(\frac{s}{r_1}\right) Re_r} \quad (\text{Regime I}) \quad (16a)$$

$$C_f = \frac{3.7\left(\frac{s}{r_1}\right)^{0.1}}{Re_r^{0.5}} \quad (\text{Regime II}) \quad (16b)$$

$$C_f = \frac{0.08}{\left(\frac{s}{r_1}\right)^{0.167} Re_r^{0.25}} \quad (\text{Regime III}) \quad (16c)$$

$$C_f = \frac{0.0102\left(\frac{s}{r_1}\right)^{0.1}}{Re_r^{0.2}} \quad (\text{Regime IV}) \quad (16d)$$

If the rotating disk acts like a centrifugal pump, the torque coefficient increases with the increasing spacing ratio (Regimes II and IV). In Regimes I and III, the pumping effect does not occur and the torque coefficient decreases when the spacing ratio increases.

In electric machines, the spacing ratio of the rotor ends is practically always higher than 0.05. This means that the pumping effect occurs in the end-winding space. Therefore, the torque coefficient should be determined according to the equations for Regimes II or IV. The spacing ratio in axial magnetic bearings is around 0.007. Figure 4b suggests that the flow is in this case in Regime I or III.

Equations 16a-16d are not valid if the disk rotates in free space. In such a case, the torque coefficient is (Kreith 1968)

$$C_f = \frac{3.87}{Re_r^{0.5}} \quad (Re_r < 3 \times 10^5) \quad (17a)$$

$$C_f = \frac{0.146}{Re_r^{0.2}} \quad (Re_r > 3 \times 10^5) \quad (17b)$$

2.3 Measurement of losses in the air gap

Introduction

The friction and gas-flow losses were studied experimentally. The analysis was focused on the motor air gap where a large part of these losses are located. The friction coefficient in the air gap was calculated based on Eqs. 14 presented by Bilgen and Boulos (1973). The gas-flow losses were analysed according to Eq. 15 (Polkowski 1984).

The friction loss in the air gap follows the equation

$$P = k_1 C_f \rho \pi \omega^3 r_1^4 l \quad (18)$$

where the friction coefficient C_f is defined by Eqs. 14 and k_1 is the roughness coefficient. It is 1.0 for smooth surfaces. The roughness coefficient is expected to be constant. However, if the roughness size is large enough to penetrate the viscous sublayer, the roughness coefficient depends on the Reynolds number in such a way that the product $k_1 C_f$ is independent on Reynolds number (see Fig. 8 by Theodorsen and Regier 1944). This means that the roughness coefficient is expected to increase when the Reynolds number increases.

There does not exist any complete research concerning the effect of rough air-gap surfaces on the friction losses. This is the case in electric motors which may have stator slots and axial as well as tangential grooves on the rotor. Some estimation of the effect of a rough rotor can be made based on the study by Theodorsen and Regier (1944). The friction loss of a rough rotor was 2-4 times

higher than the loss of a smooth rotor. One should remember that the measurements were carried out without the stator. Larjola et al. (1991a) have measured friction losses in the air gap of a high-speed generator. Both air-gap surfaces had axial grooves. They obtained a roughness coefficient of about 2.5, which is comparable with the results by Theodorsen and Regier (1944).

As discussed earlier, large losses may be associated with the coolant flow through the air gap of a high-speed motor. Based on Eq. 15, we can express the gas-flow losses by equation

$$P = \frac{2}{3} \pi \rho (r_2^3 - r_1^3) v_m u_m \omega \quad (19)$$

Equation 19 assumes that the coolant flow does not have a tangential velocity component before entering the air gap. The final tangential velocity is related to the peripheral speed of the rotor.

$$u_m = k_2 u_1 \quad (20)$$

where k_2 is the velocity factor. If we assume that both the air gap surfaces are smooth, we obtain a value of 0.48 for the velocity factor (Polkowski 1984, Dorfman 1963). This is, however, a purely theoretical value. If the rotor is rough and stator is smooth, the factor can be expected to increase. Respectively, the factor decreases if the rotor is smooth and stator is rough. Deep stator slots reduce the loss in Eq. 19 in another way, as the gas flowing along the axial slots is not significantly disturbed by the rotor rotation. By assuming that the air gap is very small, ($r_1 \rightarrow r_2$), Eq. 20 can be written into more practical form

$$P = k_2 q_m (\omega r_1)^2 \quad (21)$$

where q_m is the mass flow rate of air-gap gas.

The aim of the experiments was to measure the roughness coefficient k_1 and velocity factor k_2 in the air gap of our high-speed electric motor. The motor has a smooth rotor surface and slotted stator surface.

Method of measurement

The study was focused on the losses in the air gap region. This means that the air-gap losses were separated from the other friction losses. The separation was done by comparing the results from deceleration tests for air- and R134a-cooled motors. R134a is a refrigerant gas which is much heavier than air (Table 2). This measurement method has been reported earlier by Larjola et al. (1991b).

Figure 5 presents a construction of the test machine. The motor is cooled by blowing the cooling gas through the air gap, and the bearings have their own cooling system. The separation of the friction losses in the air gap is based on the variation of the air-gap gas, while the bearing

conditions are kept the same. By assuming that the gas properties affect the losses as stated in Eq. 18, we obtain the friction losses in the motor air gap. We used air and a refrigerant gas R134a in our measurements. These gases were selected as their densities differ greatly from each other. In the following, the procedure to evaluate the friction losses in the air gap is explained in detail. The gas properties and test conditions are presented in Table 2.

Table 2. Physical properties of air and R134a (50°C and 1.013 bar) and operation conditions of the test machine.

Property or flow condition	Air	R134a
Density [kg/m ³]	1.093	3.86
Dynamic viscosity x10 ⁻⁶ [Ns/m ²]	19.6	13.8
Rotation speed [1/s]	500–1150	500–1150
Rotor surface speed [m/s]	112–256	112–256
Couette Reynolds number x10 ⁴ (Eq. 1)	1.2–2.6	6.2–14.2
Flow rate [m ³ /min]	0–4.1	0.3–1.2
Axial gas velocity [m/s]	0–74.5	4.7–21.8
Axial Reynolds number x10 ³ (Eq. 3)	0–16.7	5.2–24.2

The test machine is accelerated into the desired rotation speed, and the power supply is switched off. The power of the decelerating rotor is

$$P = J\omega \frac{d\omega}{dt} \quad (22)$$

where J is the moment of inertia of the rotor and t is the time instant.

The pressure and temperature conditions in the air gap may vary in different deceleration tests. This naturally affects the friction powers. In order to make the test results comparable, the obtained powers P are corrected to deceleration powers P' at the reference temperature and pressure in the air gap. The power has the equation

$$P' = P + k_1 (P_{C,\text{ref}} - P_C) \quad (23)$$

where k_1 is the roughness coefficient, and $P_{C,\text{ref}}$ as well as P_C are the calculated friction powers for smooth surface (Eq. 18) in the reference and measured conditions, respectively.

Deceleration tests are carried out at different flow rates of air and R134a. Equation 19 suggests that the gas flow loss is directly proportional to the flow rate of the cooling gas. At each rotation speed, therefore, a straight line is fitted to the powers P' and the measured gas flow rates. By using

the slope of the fitted line, we can calculate the velocity factor k_2 with Eqs. 19 and 20. The friction powers at zero flow rates are marked with terms P'_{air} and P'_{R134a} .

On the other hand, we can write at each rotation speed

$$P'_{\text{R134a}} - P'_{\text{air}} = k_1 \left(P_{\text{CR134a,ref}} - P_{\text{Cair,ref}} \right) \quad (24)$$

where $P_{\text{CR134a,ref}}$ and $P_{\text{Cair,ref}}$ are the calculated friction powers for smooth surfaces (Eq. 18) in reference conditions of R134a and air, respectively. The iteration with Eqs. 23 and 24 gives us the roughness coefficient k_1 in the air gap.

Test machine

The measurements were carried out with a high-speed induction motor, originally constructed for testing of tilting pad gas bearings. Figure 5 presents the construction and main dimensions of the machine. The diameter and length of the rotor are 71 mm and 200 mm, respectively. The inner diameter of the stator core is 75 mm, thus, the radial air-gap length is 2.0 mm.

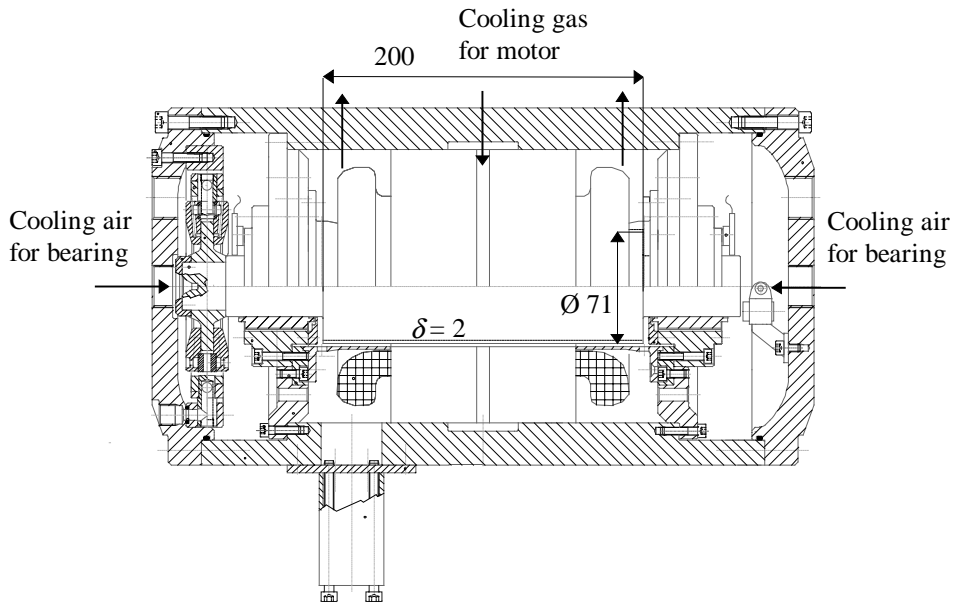


Figure 5. Constructional picture of the test machine. The solid-rotor induction motor is equipped with gas bearings.

The cooling of the test machine is illustrated in Fig. 6a. The cooling gas is blown into the motor through a cooling duct in the middle of the stator core. After passing the air gap, the hot gas is taken radially out from the end-winding space. In the experiments, the motor was cooled either by air or the refrigerant gas R134a. The cooling air was provided by a separate fan driven by a frequency converter. In R134a cooling, the gas was supplied from a pressurized gas bottle. The gas bearings have air cooling. The inlets for the cooling air are at the ends of the machine. The cooling was

maintained by a regenerative blower. Pressurized air is supplied for the axial bearing. The cooling gas for the bearings and the motor is taken out through the same outlet passages.

One aim of the investigation was to determine, does the surface roughness caused by the stator slot openings affect the friction losses in the air gap. For this reason, the measurements were done by two stator slot constructions shown in Fig. 6b. The term "Open stator slots" refers to the original construction, in which there were 36 axial grooves on the stator surface. The width and depth of the grooves are shown in the figure. The variation in the depth is due to the windings in the slots. After the tests with the original construction, the axial grooves were filled with industrial cement, and the tests were repeated. In this report, this stator construction is referred as "Closed stator slots".

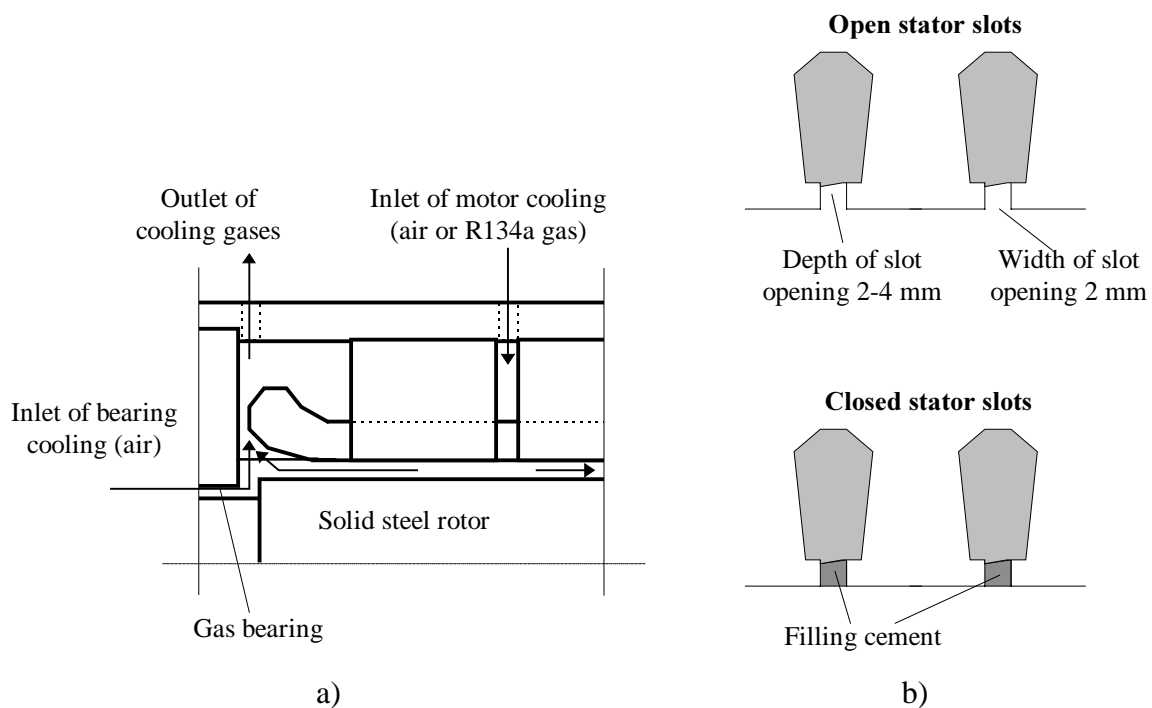


Figure 6. a) Schematic drawing of the test machine. The cooling of the electric motor is provided by a gas flow (air or R134a) through the cooling duct and air gap. The cooling gas is mixed with the bearing coolant (air) in the end of the rotor. b) Open and closed stator slots.

Measurement equipment

More than 30 deceleration tests were carried out with the test machine. During each experiment the following data was collected (sampling frequency 1 Hz) to a PC via a IEEE-488 bus.

- Time instant
- Rotation speed of the rotor
- Temperatures at the inlet of the cooling gas, in the air-gap flow, and in the end-winding space
- Flow rate of the air/weight of the R134a bottle.

Before each test, the ambient pressure was recorded. The inlet pressure of the cooling gas was noted manually at the beginning and at the end of each test. The mean value of these two figures was assumed to represent the pressure in the air gap.

The flow rate of the cooling air was measured by an orifice plate. A pressure transmitter was used to produce a voltage signal proportional to the pressure difference across the plate. This voltage was then measured by a datalogger connected to the IEEE-488 bus. The error in the flow-rate measurement is less than 1%.

The mass flow rate of the R134a gas was determined according to the loss of weight of the pressure bottle. During measurements, the bottle was hanging in a special rack. The weight of the bottle was measured by a strain gauge connected to a voltage transducer. The voltage was then measured by a digital voltmeter connected to the IEEE-488 bus. The largest errors in the measurement were caused by the swinging of the gas bottle and the varying flow rate in the gas passages to the test machine. We assume that the error in the mass flow rate was less than 2%.

Temperatures were measured with calibrated thermocouples. They were installed in the inlet and outlet of the cooling gas flow, in the air-gap flow, stator end winding and gas bearings. The ambient temperature was also measured. All the thermocouples were connected to the datalogger. The error in the temperature measurement is expected to be less than $\pm 1^\circ\text{C}$.

The inlet pressure of the cooling gas was measured with a water manometer. The pressure varied according to the gas flow rate and the rotation speed. The highest overpressures measured were around 0.05 bar. The measured values are expected to be within $\pm 1\%$ of the real ones. The ambient pressure was measured with an electric barometer device. Its error limit is ± 1 mbar.

The rotation speed of the rotor was detected by a Hall sensor. The pulses given by the sensor were counted by a digital counter connected to the IEEE-488 bus. The errors in the measured values are less than 0.5%.

Discussion of possible error sources

In addition to the instrument errors, there are some error sources in the measurement method itself, which may affect the test results. One is associated with the remanence magnetism of the rotor. The core loss is approximately proportional to the square of the stator voltage. If we assume that the core loss is less than 1 kW with a supply voltage of 400 V, the core loss is only 1.4 W with 15 V. We measured that the stator voltage decreased to 15 V in a couple of seconds after switching off the supply voltage. The core loss is very small compared with the total friction losses and, therefore, we can neglect the effect of the remanence in the results.

Another error source is related to the evaluation of the mass flow rate of the R134a gas. The gas flow rate was not constant in the tests. This was due to the freezing of the gas bottle as a large amount of gas was released into the air. For this reason, an exponential curve was first fitted to the collected weight-time data, and the mass flow rate of R134a was then derived analytically.

We assumed, that the bearing losses did not vary when we changed the air-gap gas from air to R134a. This was ensured by keeping the pressure of the static bearing at the same level (1.5 bar)

through all the measurements. In addition, the air-cooling of the radial bearings was maintained constant through all the tests.

The friction powers obtained were corrected according to the measured temperature and the pressure in the air gap. Although the thermocouple itself is a rather accurate sensor, we cannot be sure if it has indicated the mean gas temperature. The air-gap pressure was assumed to be the mean value of the inlet and outlet pressures of the cooling gas. A more accurate pressure estimate would require a sensor in the air gap or knowledge of all the pressure losses in the gas passage.

The turbulence due to the roughness on the stator surface was assumed to extend into the bushing region too. This is probably the case as the axial gas flow was towards the end-winding space. On the other hand, it has to be considered as one source of error. In addition, the flow conditions in the middle of the air gap differs surely the conditions in the other region because there the radial gas flow collides the rotor surface.

2.4 Comparison between measured and calculated results

At first, the experiments were carried out with the original machine construction. Then, the stator slots were filled with industrial cement, and the tests were repeated. The aim was to see if the filling has any effect on the friction losses. With both stator-slot constructions, several flow rates of cooling gas were used in the measurements. One deceleration test was performed without any axial air flow through the air gap. It was not possible to run the machine with very low flow rate of R134a because of too high temperatures in the cooling gas. The plastic bushings limited the operation temperatures below 120°C. The physical parameters of the gases, rotation speeds, flow rates, etc. used in the experiments are shown in Table 2.

Friction losses and roughness coefficient

Figure 7a compares the measured and calculated friction losses in the motor air gap. The friction losses are calculated by Eq. 18 with a roughness coefficient of 1.0. The cooling gas is air. At rotation speeds above 600 m/s, the measured losses are from 10% to 25% higher than the calculated losses. Compared with the case of open stator slots, the filling seems to slightly decrease the friction losses in the air gap. The difference, however, is only marginal. All the measured points fit to the same curve relatively well. This indicates that the random error sources discussed earlier did not significantly affect our measurement results.

By using the measured losses, the roughness coefficient k_1 was calculated. The results are presented in Fig. 7b. When the stator slots are open, the average roughness coefficient is 1.25 at rotation speeds 600–1100 1/s. The corresponding figure with filled stator slots is 1.13. The error limits for both the roughness coefficients are less than ± 0.10 . One has to remember that the calculated friction loss is based on an experimental equation which also has some error marginal. In

both cases, the roughness coefficient increases slightly when the rotation speed, i.e. Reynolds number increases. This was an expected result as discussed earlier.

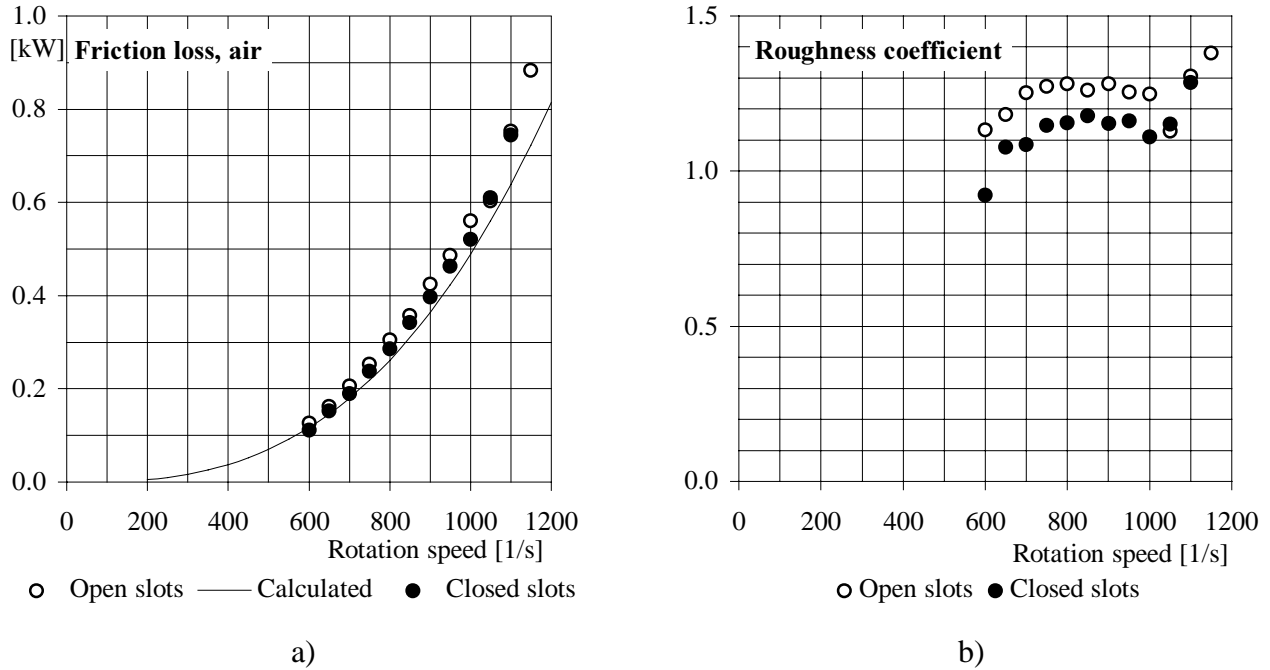


Figure 7. a) Friction losses and b) roughness coefficient in the air gap of the air-cooled motor. The coolant flow is zero. The roughness coefficient is 1.0 in the calculated friction-loss curve. The curves correspond to a temperature of 50°C and pressure of 1.013 bar in the air gap.

Compared with the losses with rough rotors (Larjola et al. 1991), the roughness due to the open stator slots increases only slightly the friction losses in the air gap. The influence is even smaller if we fill the stator slots. On the other hand, the filling of the stator slots is a slow manufacturing process and it decreases the heat-transfer from the stator to the air-gap gas. For these reasons, open stator slots are recommended for high-speed electric machines.

Gas flow losses due to axial flow

The aim of the measurements was to determine the velocity factor k_2 in Eq. 20. For this reason, several deceleration tests with different flow rates of R134a were carried out. Figure 8b presents the measured total friction powers for the R134a-cooled machine at 600, 800 and 1000 1/s. Straight lines were fitted to the friction power-flow rate data in order to obtain the friction losses due to the rotor rotation. At 1000 1/s, this power is 2 kW and the loss due to the axial gas flow is up to 0.4 kW.

By using the fitted powers, the velocity factors for the test machine were calculated with Eqs. 19-20. Figure 8b shows the results obtained. The mean value for the velocity factors are 0.15 and 0.18 with open and closed stator slots, respectively. The error in these figures is expected to be less than ± 0.03 . Both values differ greatly from a value of 0.48 which was found in the literature

(Polkowski 1984). On the other hand, the figures obtained agree with our earlier results (Saari 1995). The low values can be explained by the viscous sublayer, which is much thinner on the smooth rotor than on the rough stator surface. This decreases the mean tangential gas velocity in the air gap and, also, the velocity factor. Compared with open stator slots, filled slots reduce the viscous sublayer on the stator surface and the velocity factor increases.

As discussed earlier, the gas flowing along the stator slots may reduce the gas flow losses in the air gap. This aspect, however, did not affect our results because the bushings in the test machine are not grooved. In addition, the bushing length is sufficiently large for the gas flow to reach the final velocity profile in the air gap (Eq. 25 by Polkowski 1984).

Compared with theoretical figures for smooth air-gap surfaces, the stator roughness decreases the power associated with the tangential acceleration of the air-gap gas. The filling of the stator slots is not suggested as it increases the gas losses from those for a machine with open stator slots.

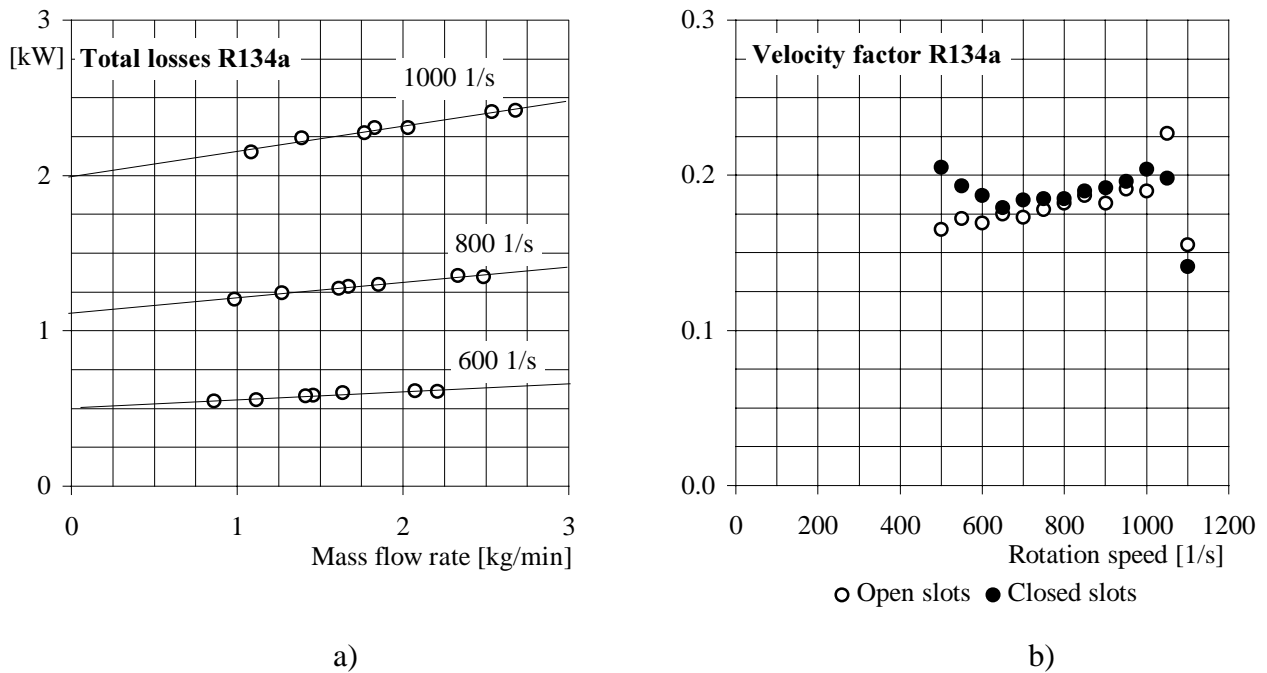


Figure 8. a) Total losses and b) velocity factors k_2 for the test machine cooled with R134a gas. The mean velocity factor is 0.15 when the stator slots are open and 0.18 when they are closed.

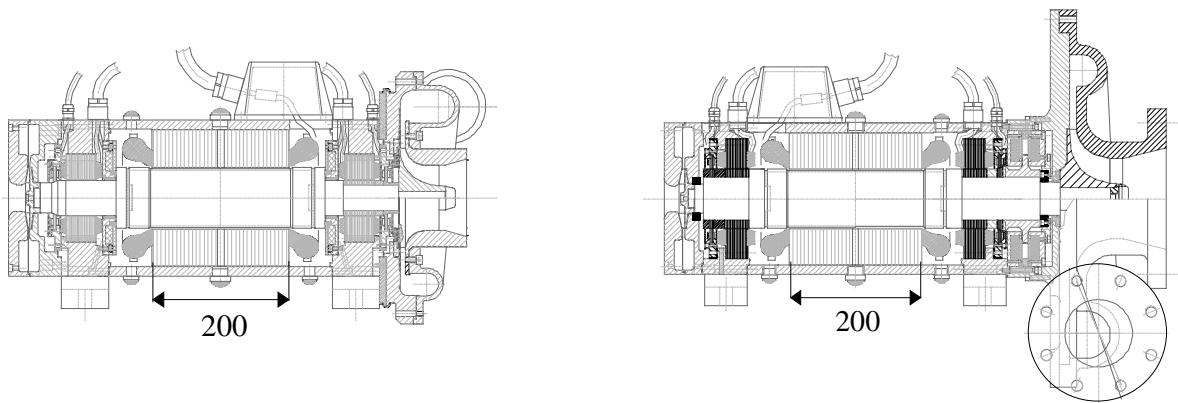
2.5 Measurement of total friction losses

The calculation of the total friction losses was verified by carrying out deceleration tests with two high-speed electric motors. Both the motors were equipped with active magnetic bearings and, the tests were performed first in normal atmospheric conditions and then in vacuum (Ueyama and Fujimoto 1990). The vacuum tests enabled the separation of the iron losses caused by the electromagnets. As a result from the subtraction, the friction losses in air were obtained.

The test machines are seen in Fig. 9. Both the motors have similar induction motors. The rotor diameter is 90 mm and the length of the stator core is 200 mm. The compressor application has smaller radial electromagnets than the vacuum pump application. In addition, the axial magnetic bearing construction are different for the machines. The impellers of the turbomachine and cooling fan were disconnected before the deceleration tests.

The measured and calculated friction losses for the test machines are presented in Fig. 10. The equations used in the calculations and the different loss components are shown in Table 3. The losses are higher for the vacuum pump because of larger magnetic bearings. In the calculations, the air gap region of the motor and radial magnetic bearings were considered as rotating cylinders in enclosures (roughness coefficient = 1.25). The clearance between the rotor end ring and stator end winding as well as all the shafts were analysed by using equations for free cylinders. The friction losses for the axial magnetic bearings were calculated by equations for rotating disks in enclosures.

As one can see in Fig. 10, the calculated total friction losses agree relatively well with the measured ones. It is a surprise, that neither the laminated rotor construction nor the stator construction of the radial magnetic bearing increase the friction losses in the machine. One can conclude that analytical equations presented earlier can be used for high-speed electric machines, in which the rotor is smooth and stator is rough. Table 3 presents the calculated friction loss components for the motors at 500 1/s. In addition, the total calculated losses are compared to the measured ones.



Air compressor, 60 kW, 42 000 rpm

Vacuum pump, 65 kW, 31 000 rpm

Figure 9. Constructions of the test machines.

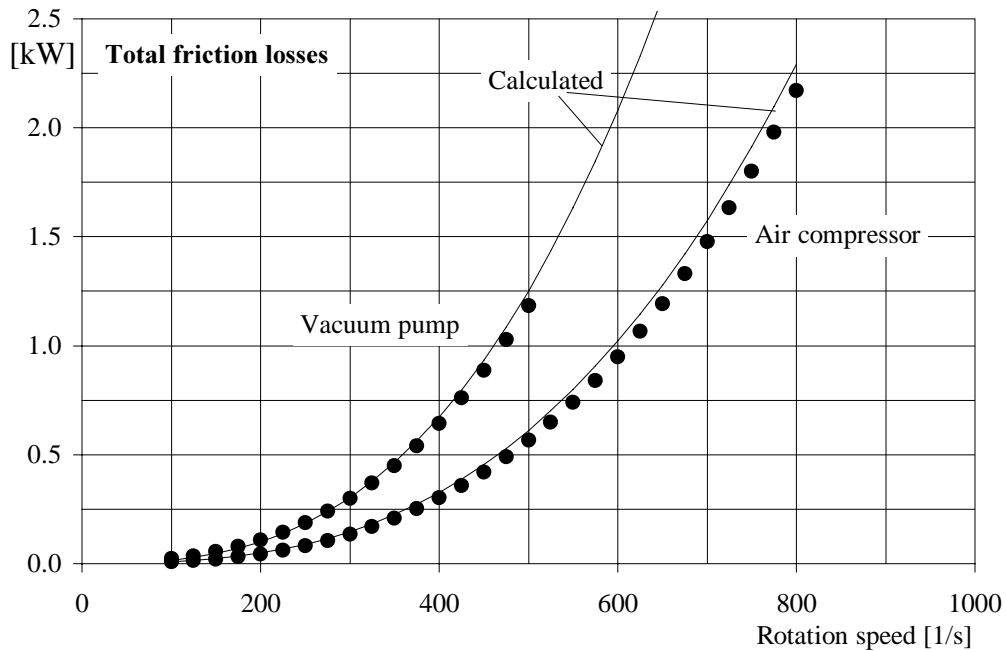


Figure 10. Total friction losses of the test machines. The solid lines represent calculated losses. A roughness coefficient of 1.25 is assumed in the electric motor and radial bearing air gaps.

Table 3. Calculated friction loss components of the two high-speed electric machines at 500 1/s.

Loss component	Model	Air compressor	Vacuum pump
Air gap	Enclosed cylinder (Eqs. 8 and 14)	222 W	222 W
End rings	Free cylinder (Theodorsen and Regier 1944)	295 W	339 W
Radial magnetic bearings	Enclosed cylinder (Eqs. 8 and 14)	27 W	138 W
Axial magnetic bearings	Enclosed disk (Eqs. 9 and 16)	33 W	270 W
Shafts, disks, rotor ends	Eqs. 8,9, 14, 16 and 17	38 W	282 W
Total calculated losses		615 W	1251 W
Total measured losses		566 W	1185 W

2.6 Discussion

Friction and gas-flow losses in high-speed electric machines are due to the rotor rotation and the cooling gas blown through the air gap. Both loss components are important to know as they decrease the efficiency and heat the motor.

The friction losses in the air gap can be calculated using analytical equations. The stator roughness caused by the stator slots increases the friction losses only by 25% compared to the losses

for a smooth stator surface. A rough rotor surface is not recommended as it increases greatly the friction losses in the air gap.

The gas losses increase when there is a coolant flow through the air gap. This loss is proportional to the velocity factor which depends on the mean tangential gas velocity in the air gap. According to the literature, the velocity factor is 0.48 (Polkowski 1984) when both the air-gap surfaces are smooth. Our experiments with a smooth rotor and rough stator gave much lower factors, from 0.15 to 0.18.

Open stator slots and a smooth rotor surface are recommended in high-speed electric machines. The stator slots affect only slightly the friction losses in the air gap. On the other hand, open stator slots improve the heat transfer in the air-gap region because of the increased turbulence and cooling surface. Thus, the advantages from the open stator slots are surely higher than the disadvantages. In addition, a rough stator decreases the losses associated with the coolant flow through the air gap.

The calculated total friction losses agreed well with the measured ones in the two high-speed electric motors tested. It seems that one can estimate the friction losses of the whole rotor with the analytical equations for the rotating cylinders and disks.

3 THERMAL MODELLING OF HIGH-SPEED INDUCTION MACHINES

3.1 Aim of the study

High-speed electric machines are used in many applications. The high power densities and the varying operation conditions place heavy requirements on the cooling of these machines. The loss distribution of an electric motor changes when its rotation speed is increased. At higher rotation speeds, most of the losses are due to gas friction in the air space and the relative share of the electric losses is diminished. This kind of loss distribution favours the use of open-circuit cooling. The coolant flow through the machine keeps the temperature difference between the motor and the air-gap gas high and, thus, provides an effective removal of the stator and rotor losses.

The wide rotation speed range and open-circuit cooling has to be taken into account in the thermal modelling of high-speed electric machines. The model has to include the calculation of the friction losses and convection heat-transfer coefficients which both vary with the rotation speed and coolant flow. In addition, the heating of the coolant flow has to be modelled.

The thermal network method was chosen for the method of analysis because of the following reasons

- Small computation time
- Equations for the friction losses are easy to include in the model
- Equations for the convection heat-transfer coefficients are easy to include in the model
- Modelling of open-circuit cooling is easy
- Thermal network is easy to construct

Perez and Kassakian (1979) have developed a detailed thermal model of a high-speed synchronous machine. For totally-enclosed induction motors, a thermal-network model has been presented, for example, by Mellor et al. (1991) and Kylander (1995). Thermal modelling of high-speed induction machines has been discussed earlier by Saari (1995). In that report, one can find a literature survey concerning thermal modelling of electric machines, a detailed description of the thermal model for high-speed induction machines and some tests results. This thesis summarises the most important aspects from the earlier report and presents some new verification results from a 235 kW high-speed motor rotating at 32 100 rpm.

3.2 Thermal-network model

Calculation principle

In the equivalent thermal network, all the heat generation in the component is concentrated in one point. This point represents the mean temperature of the component. The thermal resistances in the equivalent network are defined by demanding that the network gives the same mean temperature for the component as the analytical solution of steady-state heat transfer. The thermal models for the basic elements of electric machines have been discussed by Perez and Kassakian (1979) in more detail.

In high-speed electric machines, it is very important to locate many node points in the air space. This results from the open-circuit cooling, high friction losses and high temperature rise of the cooling gas. The coolant flow is typically heated around 60-80 K while flowing through the machine. In the thermal model, the air space has been divided into seven regions. The node points are found in the end-winding space (2 nodes), air gap, and radial cooling duct in the middle of the stator core.

The electric motor is axially divided into two parts, the drive end and the non-drive end. Two identical thermal networks are connected parallel in order to form the whole thermal model. The bearings are not included in the thermal model as their type depends on the application of the high-speed machine. The complete thermal network for the new induction motor construction (Fig. 1) is presented in Appendix A.

A computer program was developed for the solution of the thermal network. The input parameters for the program are the dimensions, material properties, rotation speed, electromagnetic losses and cooling method of the machine. In addition, some contact heat-transfer coefficients are given as input values. The convection heat-transfer coefficients and friction, as well as some cooling losses, are determined in the program. The vector of the temperature rises is obtained from the equation

$$\Delta\mathbf{T} = (\mathbf{G}_{\text{str}} + \mathbf{G}_{\text{c}})^{-1} \mathbf{P} \quad (25)$$

where \mathbf{G}_{str} is the thermal conductance matrix of the machine structure, \mathbf{G}_{c} is the cooling matrix and \mathbf{P} is the vector of the losses generating the heat. The cooling matrix is used to model the heating of the cooling gas, while flowing through the motor. The matrix contains information on the flow paths and directions of the cooling gas. Only the cooling matrix needs to be changed when one wants to test different cooling methods in an electric machine. The principle of the cooling gas modelling has been presented by Jokinen and Saari (1997).

Heat generation

The losses in electric motors can be divided into electric, friction, gas-flow and ventilator losses. The first three heat sources are located inside the motor and the ventilator losses turn into heat in the ventilator. The electric and ventilator losses are given as input values for the thermal-network program. The friction and gas-flow losses are calculated in the thermal model. Table 4 summarises the losses and the calculation methods.

The relative share of electric losses is decreased in high-speed electric machines. This results from the friction losses which increase approximately to the cube of the rotation speed. In spite of the decreased figures, electric losses remain important, because the most critical temperatures are located in the stator and rotor. The electromagnetic analyses of high-speed induction motors require numerical calculation methods because of non-sinusoidal supply frequencies and solid-rotor constructions.

The calculation of the operating characteristics of the motor is based on a time-stepping, finite-element analysis of the magnetic field (Arkkio 1987). The field is assumed to be two-dimensional. The supply voltage is imposed on the formulation through the circuit equations of the windings, which are solved together with the field equation. The rotor is rotated at each time-step by changing the finite-element mesh in the air gap, and the time-dependence is modelled by using the Crank-Nicholson method.

The electromagnetic field, currents and potential differences of the windings are obtained in the solution of the coupled field and circuit equations. The resistive stator and rotor losses are computed directly from these quantities. Estimates for the core losses are obtained from the results of the field analysis by using conventional semi-empirical methods.

In the thermal network model, friction losses heat the coolant flow in the air gap and in the end-winding space. The calculation of these losses is discussed in Chapter 2 of this report. Friction losses include the mechanical losses only due to the rotor rotation as contactless bearings are used. These losses form a significant part of the total losses because the rotor surface speed in a high-speed motor exceeds often 200 m/s. Friction losses depend on the dimensions and the rotation speed of the machine, as well as on the physical properties and velocities of the cooling gas.

High-speed motors have high loss densities and, therefore, they need open-circuit cooling. A coolant flow through the machine means that there is a static pressure difference between the inlet and outlet flows. This pressure difference depends on the physical properties and flow rate of the cooling gas, as well as the geometries of the flow passages. The needed pressure rise of the gas is provided by a ventilator. While the static pressure increases in the ventilator, the temperature of the gas increases according to the equation

$$\frac{T}{T_0} = \left(\frac{p}{p_0} \right)^{\frac{R}{\eta_p C_p}} \quad (26)$$

where p_0 and p are the static pressures in the inlet and outlet flows of the ventilator and T_0 and T are the corresponding temperatures, R is the gas constant, η_p is the polytropic efficiency of the ventilator (usually around 70%) and C_p is the specific heat. The shaft power taken by the ventilator is

$$P = q_m C_p (T - T_0) \quad (27)$$

where q_m is the mass flow rate of the cooling gas.

The needed pressure rise and the ventilator power depend on the pressure losses in the gas passages. In the high-speed electric machine, the most important pressure drops are located in the air gap and in the radial cooling duct. These pressure drops can be calculated according to Yamada (1962b) and Carew and Freeston (1967). In the end-winding space, the cross section area for the coolant flow is large, and there high flow rates are reached with low losses. The calculation of the pressure losses are not included in the thermal model as it would need iteration between parallel coolant flows.

Another cooling loss is associated with the acceleration of the cooling gas in the air gap, where the rotor forces the gas into a tangential movement. When the air gap is very small compared with the rotor radius, we can write the gas-flow loss into form

$$P = k_2 q_m (\omega r_1)^2 \quad (28)$$

By combining Eqs. 27 and 28, we can see that the heating of the coolant flow caused by the gas-flow loss is proportional to the square of the rotor surface speed. If we use a value of 0.15 for k_2 , the coolant (air) temperature rises 6, 13.5, 24 and 45 K at 200, 300, 400 and 550 m/s, respectively. This heating should be taken into account when designing the rotor main dimensions and the rotation speed.

Table 4. Estimation of losses in the thermal-network calculations.

Loss component	Calculation	Description
All electric losses	FE-program	
Friction losses in air gap	Thermal model	Empirical equation
Friction losses on end rings	Thermal model	Empirical equation
Friction losses on rotor ends	Thermal model	Empirical equation
Ventilator losses	Measured	
Gas-flow losses in air gap	Thermal model	Empirical equation

Convection heat transfer

The high-speed motors constructed are mainly cooled by the air-gap flow. In addition, the winding losses in stator are removed effectively through the end windings. These most important heat paths are shown in Fig. 11 and they are discussed in this report. All the heat paths in the thermal model have been reported by Saari (1995) in more detail.

Both the rotor surface speed and the axial gas velocity affect the heat-transfer coefficients in the air gap. A literature review concerning heat-transfer characteristics of rotating cylinders has been published by Saari (1996). The heat transfer coefficient between the rotor surface (or the stator surface) and the coolant flow has the equation

$$h = \frac{2Nu \cdot k}{\delta} \quad (29)$$

where Nu is the Nusselt number and k is the thermal conductivity of the coolant. In the thermal-network model, the Nusselt number is based on the measurements carried out by Becker and Kaye (1962)

$$Nu = 0.409Ta^{0.24} \quad (30)$$

in which the Taylor number is

$$Ta = \frac{Re_t^2 \delta}{r_r} \quad (31)$$

There are two aspects which make the use Eq. 30 uncertain in high-speed electric machines:

1. Equation 30 has been tested with Taylor numbers from 10^4 to 10^7 and it does not cover the flow conditions in high-speed electric machines (from 10^7 to 10^9). On the other hand, the flow is already fully turbulent when $Ta=10^7$, and there should not happen any changes in the flow nature at higher Taylor numbers.
2. Equation 30 does not take the axial air-gap flow into account. On the other hand, the Nusselt number increases if there is turbulent gas flow through the air gap (see Fig. 5 by Becker and Kaye 1962) and the equation gives “safe” values in the temperature rise calculations.

As with the friction coefficient, the heat transfer also depends on the surface roughness. Roughness improves heat transfer in two ways. Firstly, the cooling surface is enlarged and, secondly, the turbulence is increased. Rao (1979) has measured the heat transfer rates of rough

rotating rotors. At high Taylor numbers, the Nusselt numbers for rough rotors were up to 70% higher than the ones for a smooth rotor.

The stator winding is cooled effectively through the end windings, especially when the cooling gas is blown radially into the end-winding space. The thermal model for the end winding is essential as the loading of the motor is set by the temperatures in the stator winding.

Pickering et al. (1995) have done an experimental research dealing with the heat transfer from the stator end winding. The test motor had open-circuit cooling. The real cooling surface of the end winding is difficult to calculate because of its complex geometry. It is much larger than one can calculate by assuming the end winding shape as a toroid. The rotating rotor increases the local heat-transfer coefficient in the inner perimeter of the end winding.

In our thermal-network model, the cooling surface of the end winding is based on the shape of a toroid. The temperature field in the end-winding space is represented by two temperatures (node points 1 and 2 in Fig. 11). One is located between the end winding and frame and the other between the end winding and rotor end ring. The heat-transfer coefficients for the end winding are different for these two regions.

Near the rotor, the tangential gas velocity is much higher than the one set by the radial coolant flow. Therefore, the Nusselt number is calculated in the same way as in the air gap i.e. by using Eq. 30. On the outside perimeter of the end winding, the flow rate of the cooling gas determines the heat-transfer coefficient. We simply used the equation for a turbulent flow over a flat plate

$$Nu = 0.037 Re^{0.8} Pr^{0.48} \quad (32)$$

where Pr is the Prandtl number and the Reynolds number is determined according to the radial velocity on the end of the stator core. The calculated surface area was multiplied by a factor of 1.5 in order to take the real cooling area into account and to be still in the “safe” side in the calculations.

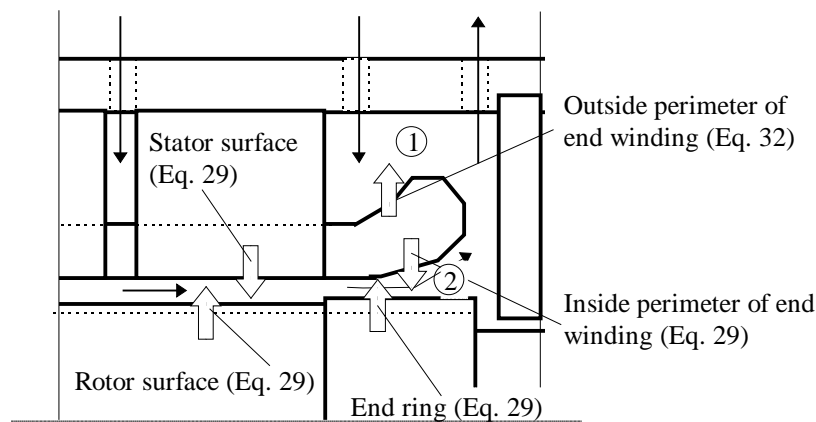


Figure 11. Calculation of the Nusselt numbers for the main convection heat-transfer paths in the high-speed electric motor.

3.3 Temperature-rise tests

Test motors

The thermal-network program was verified by tests carried out with two high-speed electric motors. Their constructions are presented in Fig. 12. Some important characteristics and dimensions of the motors are presented in Table 5.

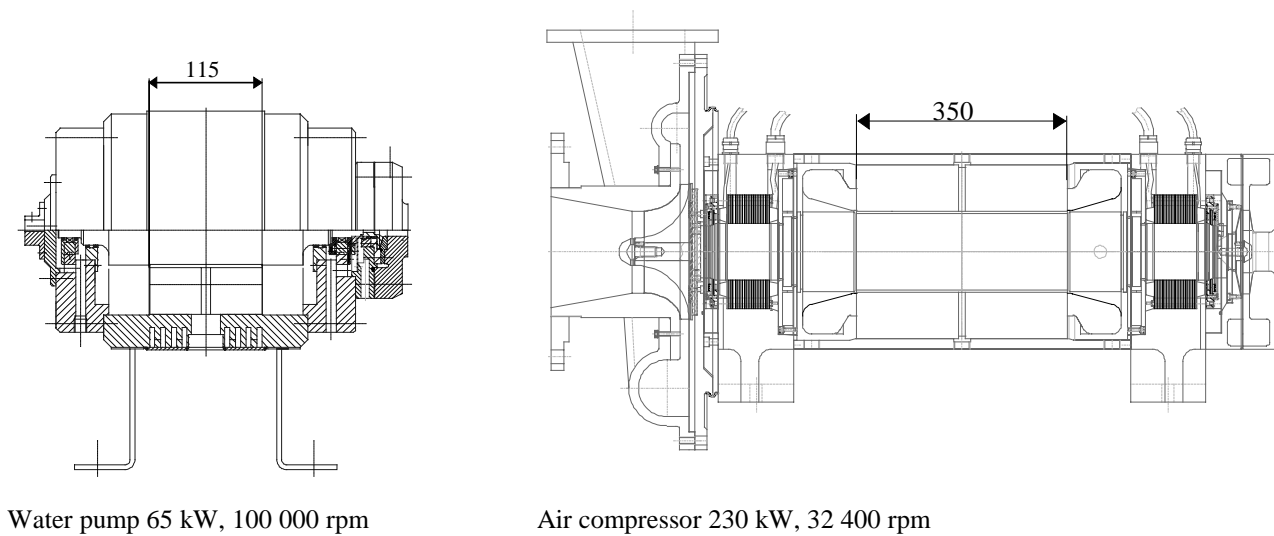


Figure 12. Constructions of the test motors. The rotor diameter is 70 mm for the water pump and 128 mm for the air compressor. The drawings are not in the same scale.

One test motor drives a water pump and the other is loaded by an air compressor. In both cases, the turbomachine has a common shaft with the electric motor. The electric motors are supplied by frequency converters in order to control the pressure rise and flow rate of the turbomachine. The water pump has water lubricated sleeve bearings and the air compressor is equipped with active magnetic bearings. The machines tested have open-circuit cooling in which the cooling air is blown through the machine. The basic motor construction is presented in Fig. 1. During the tests, the water pump motor was cooled by an external ventilator. The air compressor has its own ventilator in the non-drive end of the machine.

The machines are operated at very high speeds. The maximum speed for the water pump is 100 000 rpm which means a surface speed of 367 m/s on the rotor. The corresponding figures for the air compressor are 32 100 rpm and 217 m/s.

Table 5. Main characteristics and dimensions of the electric motors in the water pump and in the air compressor.

Parameter	Water pump	Compressor
Voltage [V]	400	400
Number of poles	2	2
Supply frequency [Hz]	1667	350–540
Power input [kW]	10–62	77–227
Length of the stator core [mm]	115	350
Rotor diameter [mm]	70	128
Load machine	water pump	air compressor
Cooling method	open-circuit, air	open circuit, air
Flow rate [m ³ /min]	2.8	16.2–25.0
Bearing type	hydrodynamic	active magnetic

Measured and calculated results

The motors were tested at several supply frequencies and powers. PWM-type frequency converters were used in the measurements. The water pump motor was operated in the field weakening area while the compressor motor was also tested at supply frequencies under the field weakening point. The loading was varied by controlling the rotation speed and throttling the outlet flow. The power inputs, voltages, currents, supply frequencies and power factors were measured by a power analyser. The rotation speed was detected by a pulse sensor. It was not possible to measure the torque of the machines because of the high rotation speed and direct coupling between the motor and the load machine. The bearing and friction losses were measured by deceleration tests.

The temperatures of the stator windings were measured by the traditional resistance method. The error limit of the measurement is $\pm 5^{\circ}\text{C}$. In the air compressor, it was possible to measure the rotor temperature by holding a temperature probe against the rotor surface after the rotor movement was stopped. There we assumed an error limit of $\pm 10^{\circ}\text{C}$. In addition, several thermocouples were installed in the air space and stators of the machines. These temperatures, however, are not very reliable because they show only local temperatures and the magnetic field disturbs the output voltage from a sensor.

Both the test motors have open-circuit cooling in which the cooling air is blown through the motor air gap. In such a cooling, the cooling air is heated due to ventilator losses before entering the motor. This heating was taken into account in the temperature-rise calculations of the motors. In the water pump, the measured inlet air temperature was used in the calculations. The inlet temperature in the air compressor was estimated by the ventilator power and coolant flow rate (Eq. 27). The ventilator power was obtained by carrying out deceleration tests, with and without the ventilator. These results are shown in Fig. 13.

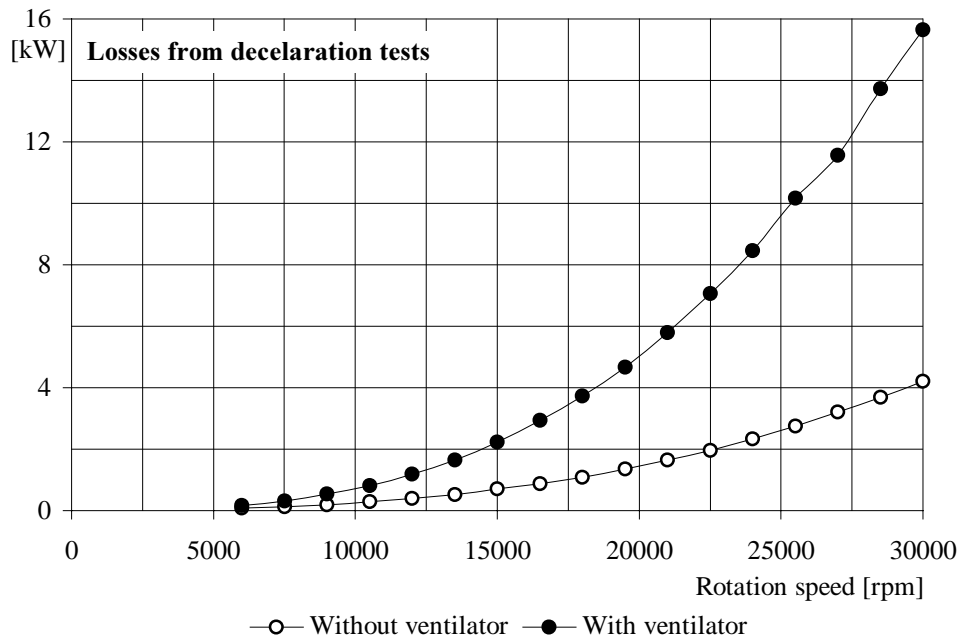


Figure 13. Measured losses of air compressor at different rotation speeds. The difference between the two curves represents the power taken by the ventilator. At 30 000 rpm, it is about 12 kW.

Before the thermal analysis, the loading points were analysed with the finite-element program. Figure 14 presents the measured and calculated currents of the test machines. In the water pump, the calculated currents are within $\pm 5\%$ of the measured ones and about the same accuracy is reached in the air compressor. There are at least two reasons which may explain the differences between the measured and computed currents. The first one is the assumption of a two-dimensional magnetic field. This is not a good approximation, especially in the end regions of the solid rotor. The second reason is associated with the modelling of iron. The magnetisation curves are assumed to be single valued. Thus, the hysteresis effects, which may be significant in hard rotors, are excluded from the analysis and, for instance, the hysteresis torque is not present in the simulated results. A small error in the current causes a larger error in the winding losses as they increase with the square of the current. As the currents and input powers are close to the measured values, we expect a relatively good accuracy in the power-loss calculation, too. A proper verification of calculated electric losses would need measurements with a back-to-back test with two identical electric motors.

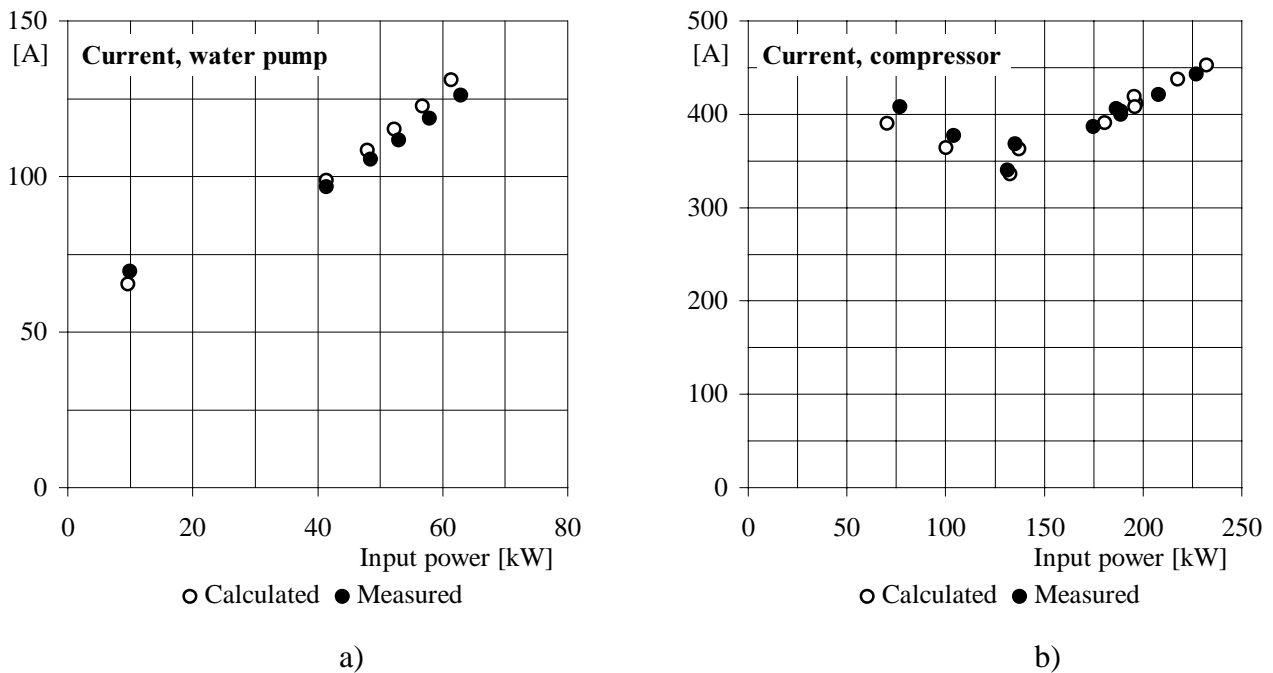


Figure 14. Stator currents of the electric motors in a) the water pump and b) the compressor.

Figure 15 presents the temperature rises in the electric motor of the water pump. The calculated power losses have been used to calculate the temperature rises. The temperatures in the stator winding and core were measured by the resistance method and a thermocouple, respectively. The supply frequency and flow rate of the cooling air were kept constant at each loading point and only the electric power was varied. The calculated temperatures increase more rapidly than the measured ones. This can be partly explained by the wrong currents shown in Fig. 14. In the highest loading point, the calculated temperature rise exceeds the measured one by 11%. In addition, the water pump motor was tested with a constant load and a variable flow rate of cooling air. These measurements have been reported by Saari (1995) in more detail.

Figure 16 presents the temperature rises in the stator winding and rotor surface of the air compressor motor. The calculated power losses have been used to calculate the temperature rises. The tests were carried out at supply frequencies 350, 400, 500, 520 and 540 Hz and the input power varied according to the rotation speed and throttling of the outlet flow. The field weakening point was set to 450 Hz in the frequency converter. The coolant flow rate increased linearly with the rotation speed, it was 25 m³/min at 540 Hz. The calculated stator temperature rises are within $\pm 8^{\circ}\text{C}$ of the measured ones. This is a satisfactory result if we take the errors in the currents and input powers into account. In the rotor, the calculated results agree within $\pm 10^{\circ}\text{C}$ with the measured ones. The machine has class F insulation which allows a temperature rise of 105 $^{\circ}\text{C}$ in the stator winding. As one can see, this limit was reached at 540 Hz when the input power was 227 kW.

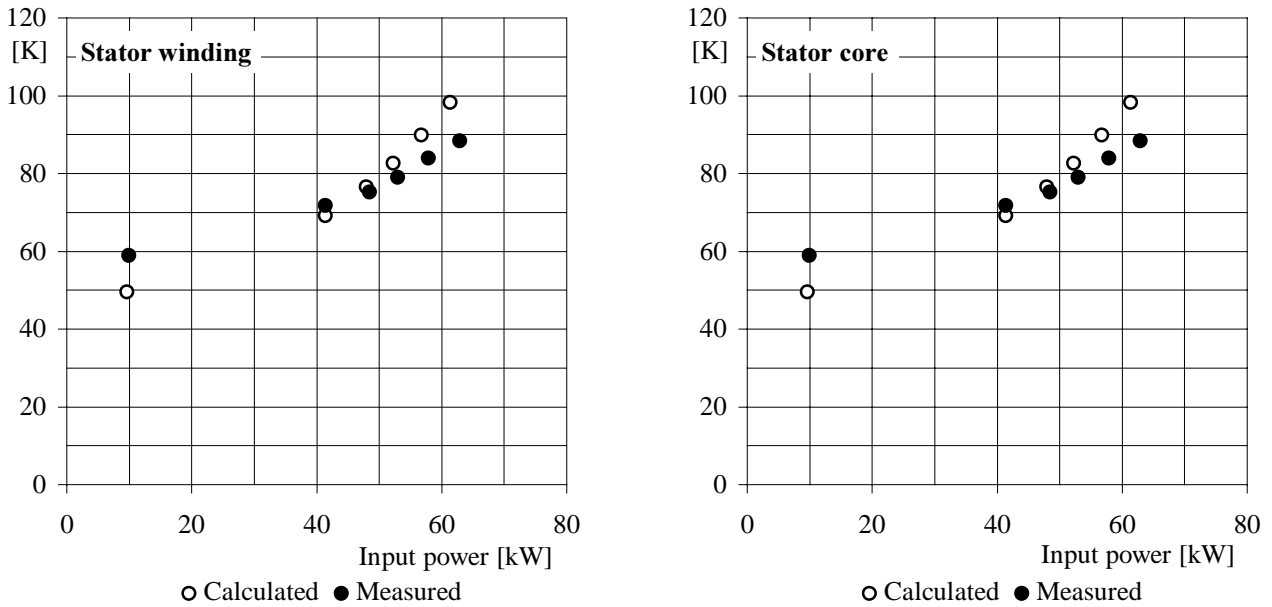


Figure 15. Temperature rises in the stator winding and core of the water pump motor. The coolant flow rate was $2.8 \text{ m}^3/\text{min}$ in all the test points. The supply frequency was 1.67 kHz .

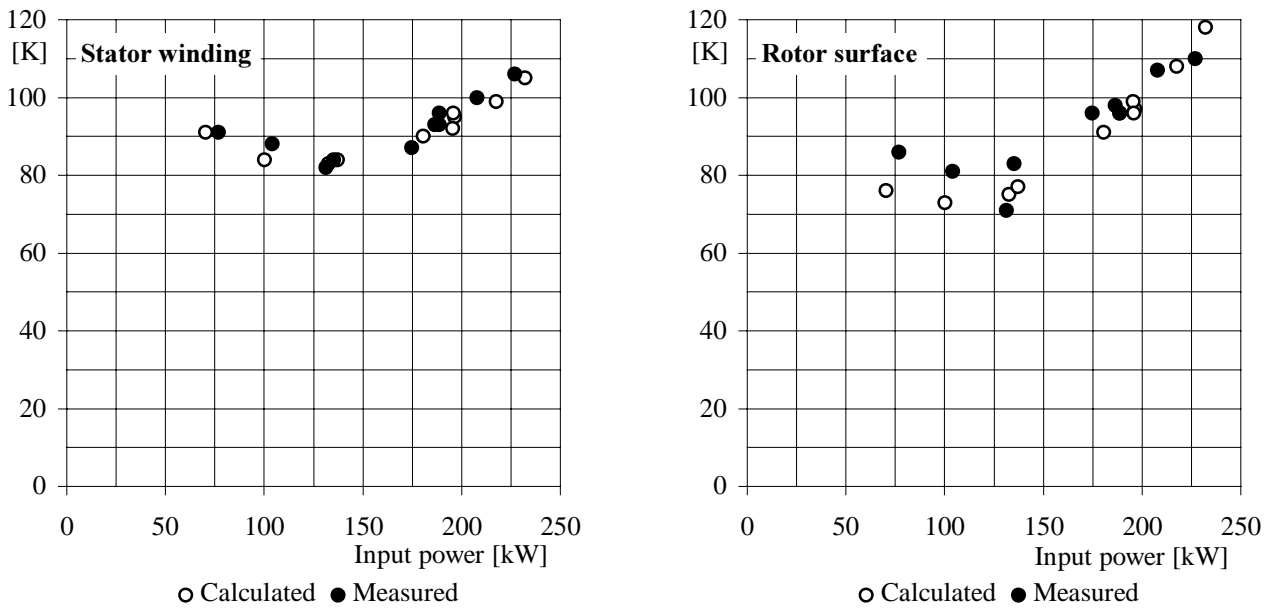


Figure 16. Temperature rises in the stator winding and rotor surface of the air compressor motor. The coolant flow rate varied between 16.2 and $25 \text{ m}^3/\text{min}$ in the test points. The supply frequency was $350\text{-}540 \text{ Hz}$.

3.4 Sensitivity of the model

In order to find the most essential aspects in the temperature-rise calculation, a sensitivity analysis for the air compressor was carried out. The loading point 218 kW and 520 Hz was selected for the

more detailed analysis and some figures in this loading point are presented in Table 6. As one can see, the ventilator power forms about 50% of the total motor losses. The ventilator losses could be decreased by improving the cooling system of the machine. About 60% of the electric losses are located in the stator and 40% in the rotor. The losses in the stator core are mainly removed through the motor frame to the ambient air and cooling air in the frame ducts. Stator winding is cooled by end-winding and air-gap flows. Nearly all of the rotor losses are located in the copper coating of the rotor. They are effectively removed by the air flows in the air gap and end-winding space.

Table 6. Calculated values for the electric motor of the air compressor at 520 Hz and 218 kW.

Parameter		Losses	
Supply frequency [Hz]	520	Total stator losses [kW]	4.50
Voltage [V]	421	Stator winding losses [kW]	2.71
Current [A]	437	Losses in stator core [kW]	1.79
Power factor	0.67	Total rotor losses [kW]	3.16
Power input [kW]	217.6		
Electric losses [kW]	7.7	Heat paths	
Friction losses [kW]	4.6	Stator ⇒ air-gap flow [kW]	1.24
Cooling losses [kW]	11.6	Stator ⇒ end-winding flow [kW]	1.58
Bearing losses [kW]	0.7	Stator ⇒ cooling-duct flow [kW]	0.17
Shaft power [kW]	193.0	Stator ⇒ frame [kW]	1.51
Flow rate of air [m ³ /min]	23.9	Rotor ⇒ air-gap flow [kW]	1.44
Temperature rise of stator winding [K]	99	Rotor ⇒ end-winding space [kW]	1.62
Temperature rise of rotor surface [K]	108	Rotor ⇒ shaft [kW]	0.10

Table 7 presents the results from the sensitivity analysis. The percentage values show how much one must vary the parameters in order to raise the winding temperature rise from 99 K to 109 K. As it was expected, the temperature rise of the stator winding is the most sensitive on the corresponding losses: an increase of 23% in the winding losses is enough to raise the temperature by 10 K in the winding. In the core losses, the needed increment is 63%. In the rotor, the losses are allowed to increase by 120% before a rise of 10 K is achieved. When the ventilator power is increased by 45%, the temperature rise of inlet air is increased by 10 K and nearly all the motor temperatures are increased accordingly. In our case, the temperatures are sensitive on the ventilator power as it forms about half of the total losses. There is not any single thermal resistance in the model which affects greatly the stator temperature. This results from the effective removal of winding losses through both the end-winding and stator teeth. When the total flow rate of cooling

air is decreased by 18%, the temperature rise of the inlet air is increased by 4.3 K (ventilator power remains constant). This together with the higher total temperature rise of the cooling air increases the stator winding temperature by 10 K. The effect of decreased convection heat-transfer coefficients and acceleration power is not essential.

The sensitivity analysis underlines the modelling of the cooling. One has to know the flow rate in each node in the thermal model relatively accurately. The ventilator power is an important parameter if the cooling gas is blown through the machine. In the machine analysed, the friction losses did not affect greatly the temperature rise in the stator winding. Its importance will rise, however, very rapidly if the peripheral speed of the rotor is increased. The stator is cooled by the air-gap flow, end-winding flow and frame. Because there are three important heat paths instead of only one path, one can not find any single thermal resistance affecting greatly the stator winding temperature. The situation is totally different in the rotor as the temperature rise is nearly directly proportional to the convection heat-transfer coefficient on the rotor surface.

Table 7. Sensitivity of the temperature rise on different parameters. The percentage value is the variation needed to increase the temperature rise of stator winding from 99 K to 109 K. Thus, a high percentage value means low sensitivity and vice versa.

Parameter	[%]
Losses in stator winding	+23
Losses in stator core	+63
Losses in rotor	+120
Friction losses in the air gap	+250
Friction losses in the end-winding space	+180
Friction losses in air-gap and end-winding space	+100
Ventilator power	+45
Thermal resistance between stator surface and air gap	+250
Thermal resistance between end winding and end-winding space	+200
Both the above two thermal resistances	+80
Contact resistance between stator winding and core	+600
Contact resistance between stator core and frame	+600
Total flow rate of cooling air	-18

3.5 Discussion

Thermal networks are effective in the cooling design of high-speed induction machines. As these machines operate between 15 000 rpm and 200 000 rpm, the thermal model should contain

equations for the friction, gas-flow and cooling losses as well as for the convection heat-transfer coefficients.

Friction losses can be estimated by semi-empirical analytical equations. Although they form a large part of the total losses, the temperature rise of stator winding is not sensitive on these losses. On the other hand, they need to be correctly estimated as they affect greatly the total efficiency of the machine.

High-speed induction machines need open-circuit cooling because of the high friction and gas-flow losses in the air space. The temperature of the coolant rises typically 60–80 K while flowing through the machine. The high temperature rise sets some requirements for the thermal-network model. First, the heating of the cooling gas has to be modelled. Second, several node points have to be located in the air space. And third, the gas flow rate has to be correct in each node point. To be exact, the last requirement means that the model should contain equations for the pressure losses in each gas-flow branch. This work was not completed in this research and the flow rates and ventilator powers were estimated according to measurements.

Convection heat-transfer coefficients are very high in high-speed machines because of the high rotor surface speed. This leads to relatively low temperature differences between the stator, air space and rotor. The calculated temperature rise of stator winding is not sensitive to the heat-transfer coefficients because the winding is rather uniformly cooled through the end windings, stator teeth and frame. The rotor losses are mainly removed by the air-gap flow. This makes its temperature rise very sensitive on the heat-transfer coefficient on the rotor surface.

The thermal model developed was tested by two high-speed induction machines. The calculated temperature rises in the stator winding and rotor deviated less than 10 K from the measured values. This accuracy is good enough for the cooling design of high-speed induction machines.

4 MAXIMUM POWER OF HIGH-SPEED INDUCTION MOTORS

4.1 Introduction

The development of high-speed electric motors has been going on for several years at Laboratory of Electromechanics, Helsinki University of Technology. The aim has been to design a motor which is suitable for series production and which can be used at powers up to several hundreds of kilowatts when the rotation speed is more than 20 000 rpm.

Figure 17 shows the operation points of some high-speed induction motors reported in literature during years 1989-1996. The referred papers are listed in Appendix B. The powers decrease rapidly with the increasing speed. This is mainly caused by the mechanical factors limiting the rotor diameter and length. The centrifugal forces are too large for conventional laminated rotors and bending critical speeds of these rotors are too low. The rotors have to be supported by magnetic or fluid bearings as conventional rolling bearings cannot sustain the speeds.

The white dots in Fig. 17 refer the solid-rotor induction motors tested at Helsinki University of Technology. The powers have been obtained by temperature-rise tests and they do not represent the maximum power of the motor type developed. The aim of this study was to estimate this maximum power. For this reason, eight motors were designed and analysed by the finite-element and thermal network methods. This chapter concentrates on the thermal and cooling aspects of the motors. The estimation of the maximum power was carried out at rotation speeds 50 000, 100 000, 150 000 and 200 000 rpm.

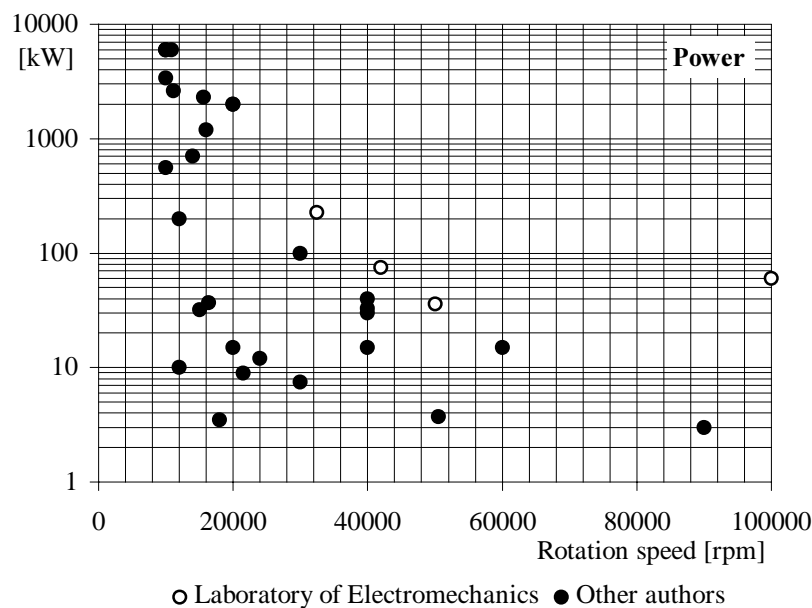


Figure 17. Operating points of high-speed induction motors reported during years 1989-1996. The white dots refer to the induction motors developed and tested in Laboratory of Electromechanics. The papers from which the data was collected are listed in Appendix B.

4.2 Construction of the high-speed motor

The power an electric machine is approximately proportional to the speed and volume of the rotor (Vogt 1983)

$$P = C_m \omega_r d_r^2 l_r \quad (33)$$

where C_m is the utilisation factor, ω_r is the mechanical angular frequency, d_r is the rotor diameter and l_r is the rotor length. The utilisation factor depends on the type, construction, speed and cooling method of the machine. Equation 33 implies, however, that the maximum power should be searched from such constructions that maximise the active volume of rotor.

The diameter of the rotor is limited by the mechanical strength of the materials, and the length by the bending critical speeds. From the mechanical point of view, rotors made of solid steel are much better than laminated rotors. Because of electrical and mechanical reasons, our machines have a rotor construction in which the solid rotor is coated with a thin copper layer. This construction is presented in Fig. 1.

The best steel sustains stresses well over 1000 MPa. The centrifugal acceleration causes this stress in a rotating cylinder when its surface speed is about 550 m/s. We have tested rotors at surface speeds of about 400 m/s (Saari 1995) and, therefore, we included these two surface speeds in our analysis.

The load machine is usually coupled directly to the high-speed electric motor shaft. The bending critical speeds depend, for instance, on the type of the bearing and the construction of the load machine. In order to keep the analysis free from a special application, the critical speeds were calculated for the rotor-bearing system without the load machine (Lantto 1997). The rotor lengths were adjusted to give a first bending critical speed that is 20% higher than the rotation speed. For a real application with the load machine connected, the rotors should be made somewhat shorter if one wants to operate under the first critical speed.

The strength of the steel-copper joint sets some additional limits to the rotor design. Table 8 gives the maximum values for the rotor dimensions set by the mechanical factors. The rotor lengths include the end-rings which are simple cylinders joined to the surface of the rotor core. Their thickness equals the maximum value allowed by the strength of the joint, and their axial lengths are such that the current density in them is half of the value in the axial conductors.

Table 8. Main dimensions of the electric motors. The dimensions are set by mechanical factors. The motor codes are used in the text when referring to motors with these parameters.

Rotor surface speed 400 m/s				
Code of the motor	n50v400	n100v400	n150v400	n200v400
Rotation speed	50 000	100 000	150 000	200 000
Rotor diameter	153	76	51	38
Rotor length	673	334	224	167

Rotor surface speed 550 m/s				
Code of the motor	n50v550	n100v550	n150v550	n200v550
Rotation speed	50 000	100 000	150 000	200 000
Rotor diameter	210	105	70	52
Rotor length	777	389	259	192

4.3 Thermal analysis of the high-speed motor

The aim of the thermal analysis was to estimate the maximum powers of the motors shown in Table 8. In this Section, the analysis of motor n100v400 is discussed in detail. The results for the rest of the motors are presented in Section 4.4.

Method of analysis

The cooling method used in the analysis is presented in Fig. 18. The cooling air is blown into the machine through a radial cooling duct in the stator core (q_{v1}) and directly into the end-winding space (q_{v2}). The pressure drops in the radial cooling duct and in the air gap are calculated according to Carew and Freeston (1967) and Yamada (1962b), respectively. The end-winding flow is supposed to have the same pressure drop as the cooling-duct flow. The heating of the cooling air in the ventilator is estimated by Eq. 26 by using a polytropic efficiency of 0.75%. The same inlet temperature was used in the cooling-duct and end-winding flows. The power of the ventilator was calculated by Eq. 27.

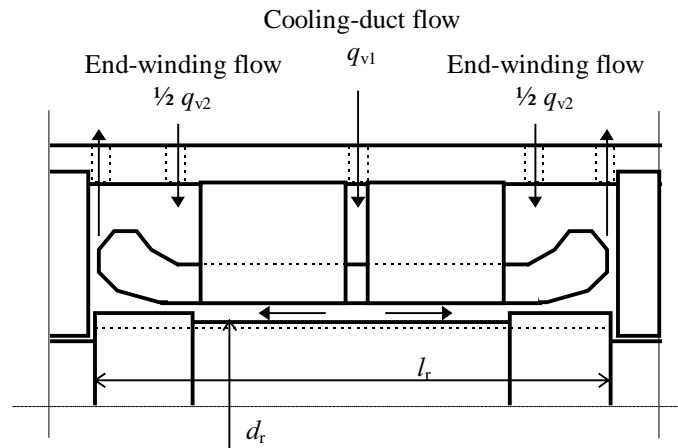


Figure 18. Cooling method of the high-speed induction motor.

The powers of the motors in Table 8 are limited by the temperature rise in the stator winding and rotor. In the analyses, the limits were 105 K (class F insulation) in the stator and 150 K in the rotor. In order to find the maximum power, the following variables were optimised:

- Cooling air flow rate
- Rotor slip and air-gap flux density
- Radial air-gap length

In each operation condition, the temperature rise of the motor as well as the friction, gas-flow and cooling losses were calculated by using the thermal-network program.

Figure 19 presents the division of the losses in the high-speed motor. The motors were judged according to the shaft power. Only the friction losses in the motor region were considered, because the losses in the bearings, shafts etc. depend on the application of the motor. The gas-flow losses appear in the motor air gap and they were included into the analysis. The cooling air was provided by an external ventilator and its losses were not included in the results.

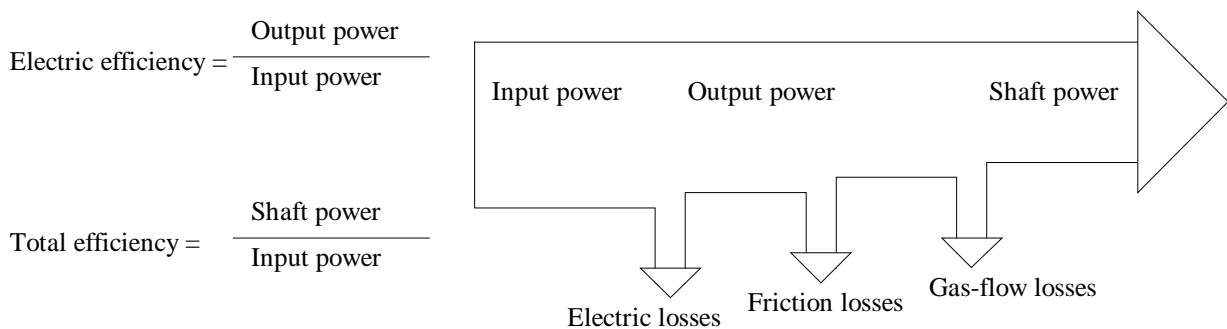


Figure 19. Division of losses of the high-speed induction motor.

Electric losses

The electric performance of the motor was computed by the finite-element program. The output powers and electric losses were calculated at different slips. Figure 20 presents the results for motor n100v400. The no-load losses are relatively high because of the high supply frequency and magnetising current. The electric losses increase approximately to the square of the output power. The air-gap flux density is around 0.36 T in the points presented.

At each slip, the output power of the motor increases when the supply voltage is increased. Because of the low air-gap flux density, the stator core is not saturated, and the power and electric losses increase proportional to the square of the supply voltage. This linear behaviour is presented by the solid line for slip 0.70%. As one can see, the same slip gives us the best electric efficiency. At higher slips the electric losses are concentrated more on the rotor than on the stator.

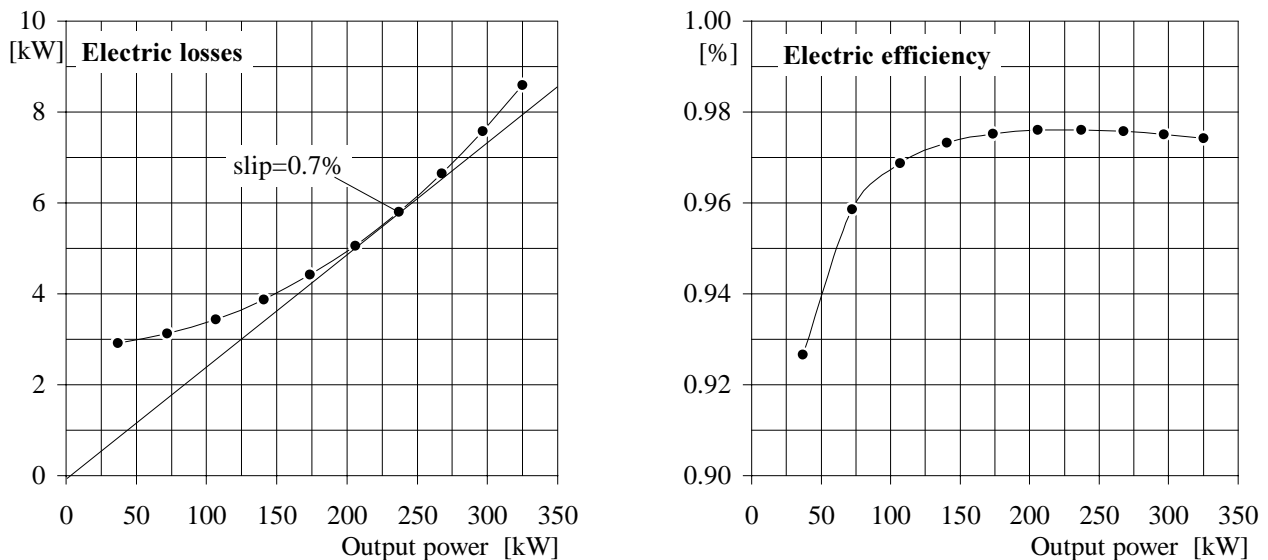


Figure 20. Electric losses and efficiency of motor n100v400. Different operation points have been obtained by keeping the supply voltage constant and varying the slip. The no-load flux density is 0.37 T and the slip is varying between 0.1 and 1.0%.

Optimisation of coolant flow

Figure 21 presents the shaft power and total efficiency of motor n100v400 operated at a slip of 0.70%. As one can see, the maximum power 235 kW is reached when the cooling-duct flow is 4.1 m³/min and the end-winding flow is 60 m³/min. The power rises more sharply at low flow rates than at high flow rates. An optimum cooling-duct flow can be found due to the following reasons. First, the heating of the air-gap gas limits the power when the flow rate is small. On the other hand, the temperature rise in the end-winding space limits the power when the flow rate is high. This follows from the high ventilator losses which heat the cooling air before it enters the machine. The best cooling-duct flow does not depend on the slip or the air-gap flux density because the friction losses set the temperature rise of the cooling air and electric losses are a minor factor. The friction

losses stay constant at different motor powers because they are determined according to the rotation speed and motor dimensions. The best efficiency of the motor (95%) is reached at a lower cooling-duct flow rate than the highest shaft power. For motor n100v400, this flow rate is 3 m³/min.

The power increases when the end-winding flow increases. This results from the increased heat-transfer coefficients and decreased temperatures in the end-winding space. The upper limit for the power is set by the thermal resistance across the winding insulation. The power increases more sharply when the cooling-duct flow rate is set to the optimum value (4.1 m³/min).

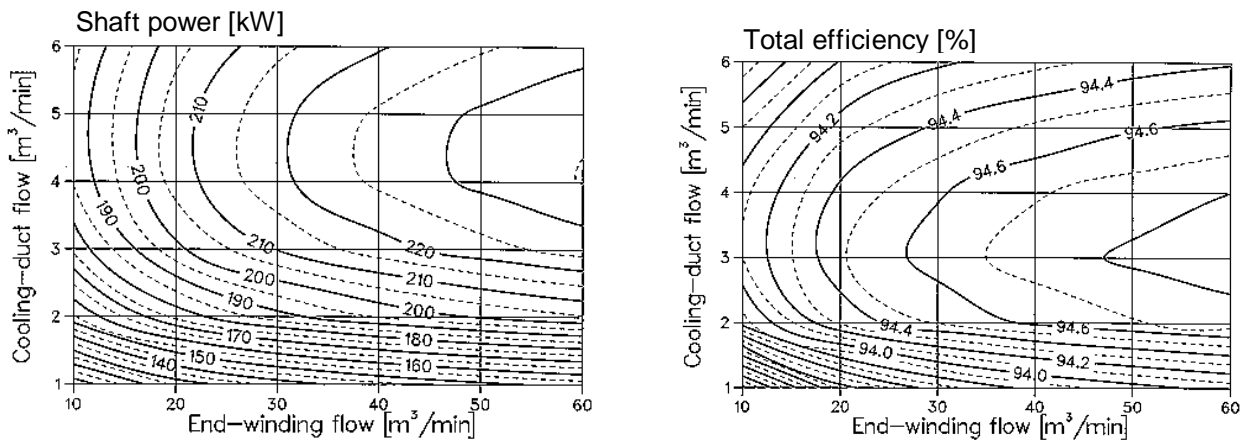


Figure 21. Shaft power and total efficiency of motor n100v400. The motor is operated at slip 0.7%.

Optimisation of slip and air-gap flux density

In addition to the flow rate, there is also an optimum slip which gives the highest power. For motor n100v400, the best slip is 0.70%. The load capacity depends on the slip as it affects the balance between the stator and rotor losses. This is presented in Fig. 22. The same power can be obtained at different slips by varying the supply voltage i.e. magnetic air-gap flux density. When the supply voltage decreases, the losses and temperature rise in the stator core decrease. If the power is kept constant, the stator current must increase. The current cannot, however, increase as much as the voltage decreases, because the winding losses affect the stator winding temperature more than the core losses. When the supply voltage is increased, the magnetising current and core losses increases. This means that very high voltages are not recommended either. As a result of these two phenomena, one can find the supply voltage and slip which give the highest power.

The above is true if the temperature rise of rotor is not critical. This was the case of motor n100v400 with a 3.0 mm air-gap length. If smaller air gaps were used, the rotor losses and temperature would become high. Then, the temperature limit may be reached earlier in the rotor than in the stator winding.

From the electric losses point of view, the best slip of motor n100v400 is 0.70%. At this same operation point, the motor reaches its highest power. The friction and cooling losses appear in air

space and they are easy to remove by a throughflow of cooling air. The flow rate should be large enough to keep the air space cool. The electric losses increase when the power is increased. The electric losses cannot be increased as freely as the losses in air space. The thermal resistance between the loss source and cooling air sets a limit for the electric losses. Therefore, the highest power is achieved at the same slip which gives us the best electric efficiency of the motor.

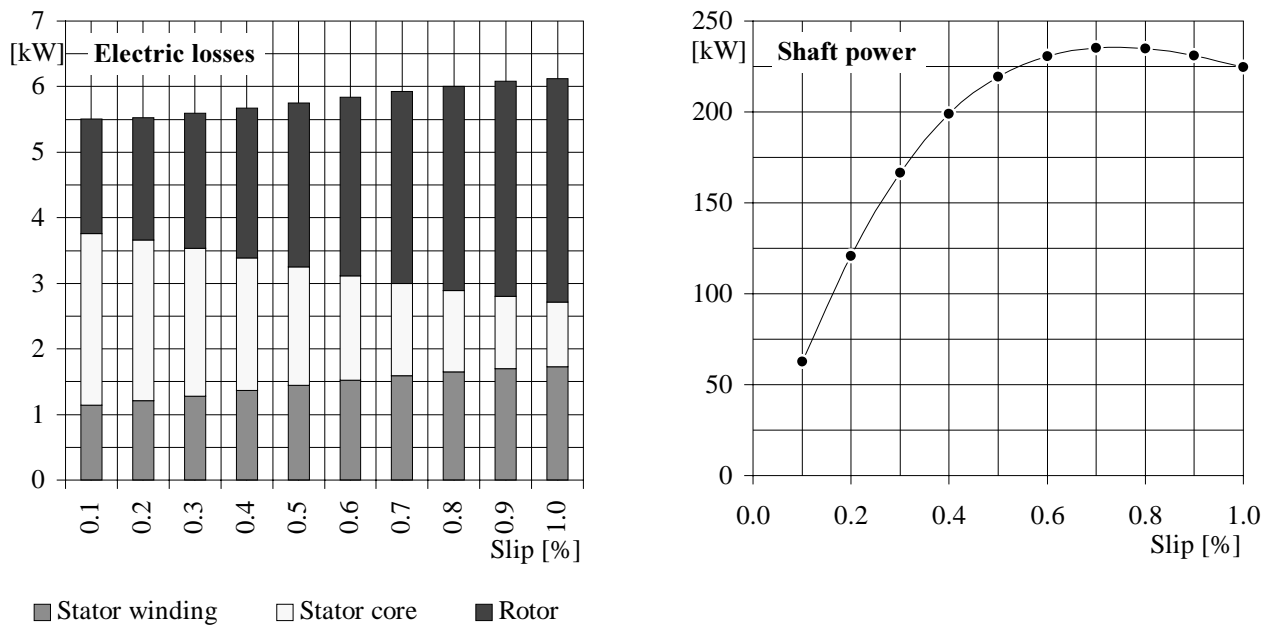


Figure 22. Variation of electric losses and shaft power of motor n100v400 operated at different slips. The values represent the maximum losses and power at each slip ($q_{v1}=4.0 \text{ m}^3/\text{min}$ and $q_{v2}=60 \text{ m}^3/\text{min}$).

Optimisation of the air-gap length

The air-gap length is an important parameter when the power of a high-speed motor is considered. The harmonics of the air-gap field cause eddy-current losses in the surface of the solid rotor. These losses can be decreased by increasing the air-gap length. On the other hand, the magnetising current and stator losses increase when the air gap is increased. The effect of the air-gap length on the electric losses and power factor is shown in Fig. 23. The shaft power is 235 kW in all the points analysed. For the total electric losses point of view, the best air-gap length for motor n100v400 is 3.5 mm.

Figure 24 shows the power curves (slip 0.70%) of motor n100v400 with the air-gap length as a parameter. The highest power, 250 kW, is obtained when the air gap is 3.0 mm and the flow rate in the duct is $4.5 \text{ m}^3/\text{min}$. With 3.0 and 5.0 mm, the power is limited by the temperature rise of stator winding. When the air gap is 2.0 mm, the rotor temperature rise (max. 150 K) limits the power to 200 kW. This results from the high rotor losses and high inlet temperature of cooling air caused by the high ventilator power.

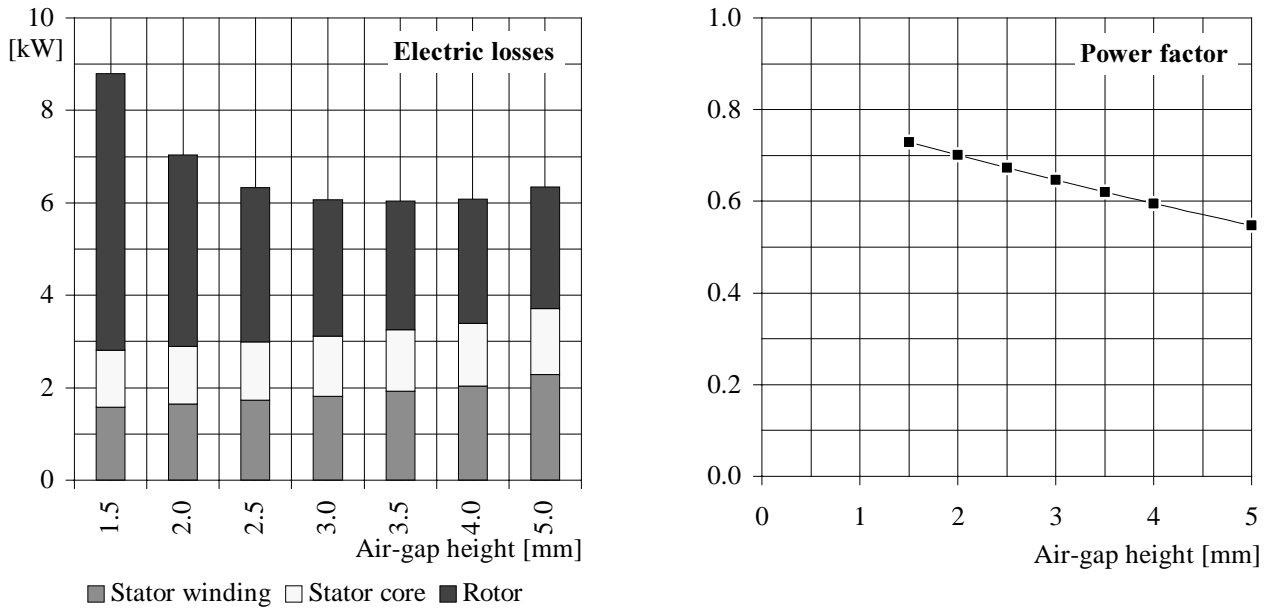


Figure 23. Electric losses and power factor of motor n100v400 at air-gap heights 1.5-5 mm. The shaft power is 235 kW.

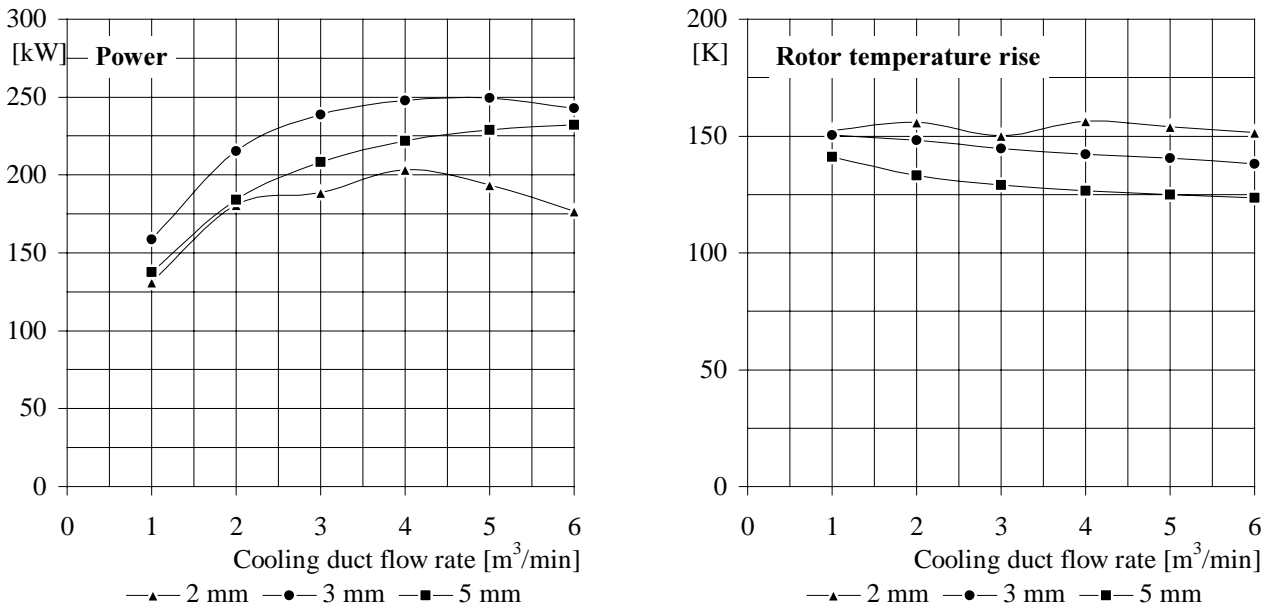


Figure 24. Maximum power and rotor temperature rise of motor n100v400 at air-gap heights 2.0, 3.0 and 5.0 mm.

4.4 Maximum powers of high-speed induction motors

Power and utilisation factor

Figure 25 shows the calculated shaft powers for the eight high-speed induction motors designed. More detailed information of the maximum-power points can be found in Appendix C. The power is approximately inversely proportional to the square of the rotation speed. The highest power was obtained with the motor n50v550, 1390 kW and motor n200v400 gave us the lowest power, 50 kW. From the maximum power point of view, the new motor construction is superior compared with the high-speed machines reported in the literature.

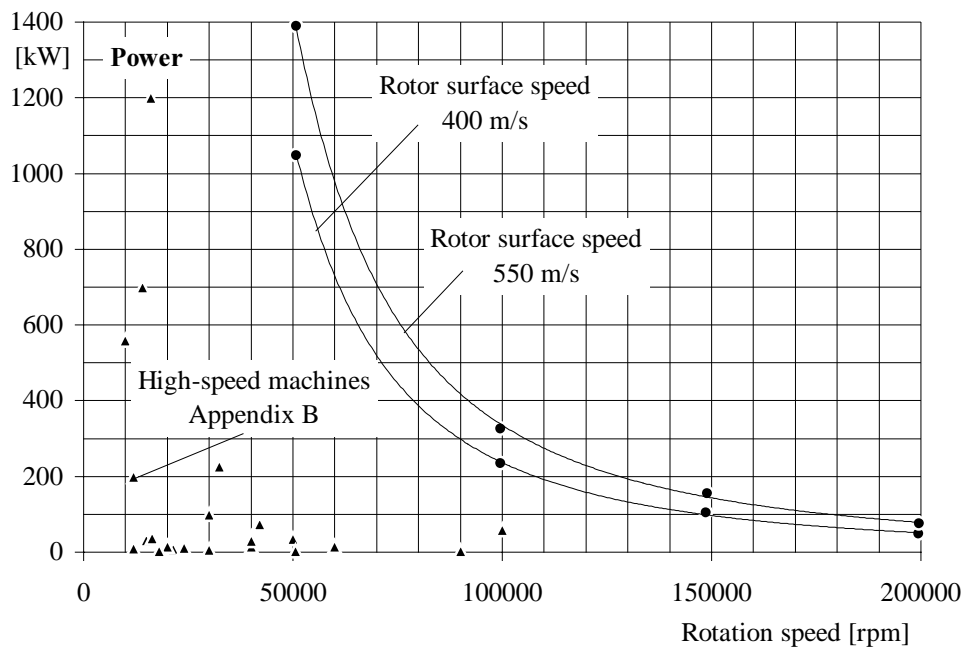


Figure 25. Maximum powers of the solid-rotor induction motors. At a rotor surface speed of 550 m/s, the power decreases with the rotation speed power 2.1. The corresponding figure is 2.2 at 400 m/s. The correlation is high between the calculated powers and the fitting curves. The machines reported in the literature (Appendix B) are marked by black triangles.

At each rotation speed, the power is proportional to the rotor diameter. This means that the utilisation factor (Eq. 33) decreases when the rotor surface speed increases. The utilisation factor is 8.7-10.1 Nm/dm³ for the motors with the rotor surface speed 550 m/s. At 400 m/s, the utilisation factor is 14.7-15.9 Nm/dm³ for three motors and 12.6 Nm/dm³ for the motor n200v400. A lower figure results from the small volume of the rotor. The utilisation factor seems to be independent on the rotation speed when the rotor surface speed is constant.

The motors are operated at air-gap flux densities 0.26-0.43 T. The slips are between 0.4% and 0.9%. The motors running at 400 m/s are operated at higher flux densities and slips than the 550 m/s motors. All the figures are presented in Appendix C.

Losses and efficiency

Figure 26 shows the loss distributions of the motors. Electric losses are generated rather equally in the stator and rotor. Electric losses form 39–55% of the motor losses when the surface speed of the rotor is 400 m/s. At 550 m/s, the friction losses naturally form a larger part of the total losses than at 400 m/s. For all the motors, the gas-flow losses are 12–22% of the total losses.

Figure 27 shows the efficiencies of the motors. The highest electric efficiency, 98.7%, was obtained with the motor n50v550. The electric efficiency decreases with the size of the motor. This can be explained by the large magnetising losses for small motors. The total efficiencies are 96–91% for the motors running at 400 m/s. Due to the higher friction losses, the figures are lower, 93–88%, when the motors run at 550 m/s.

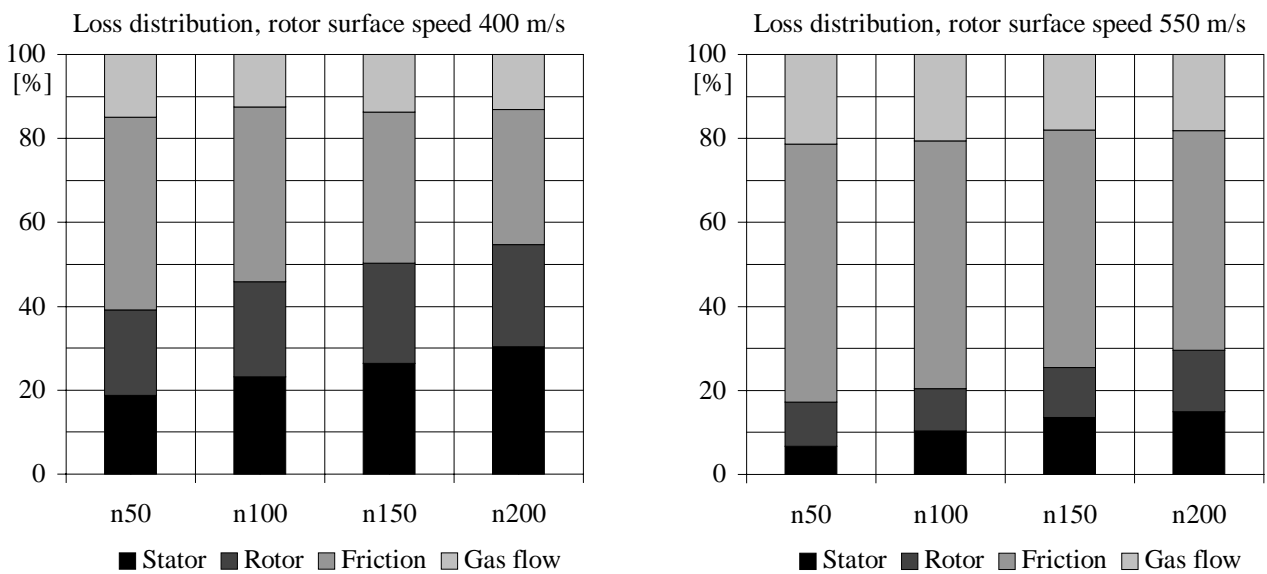


Figure 26. Loss distributions of the motors.

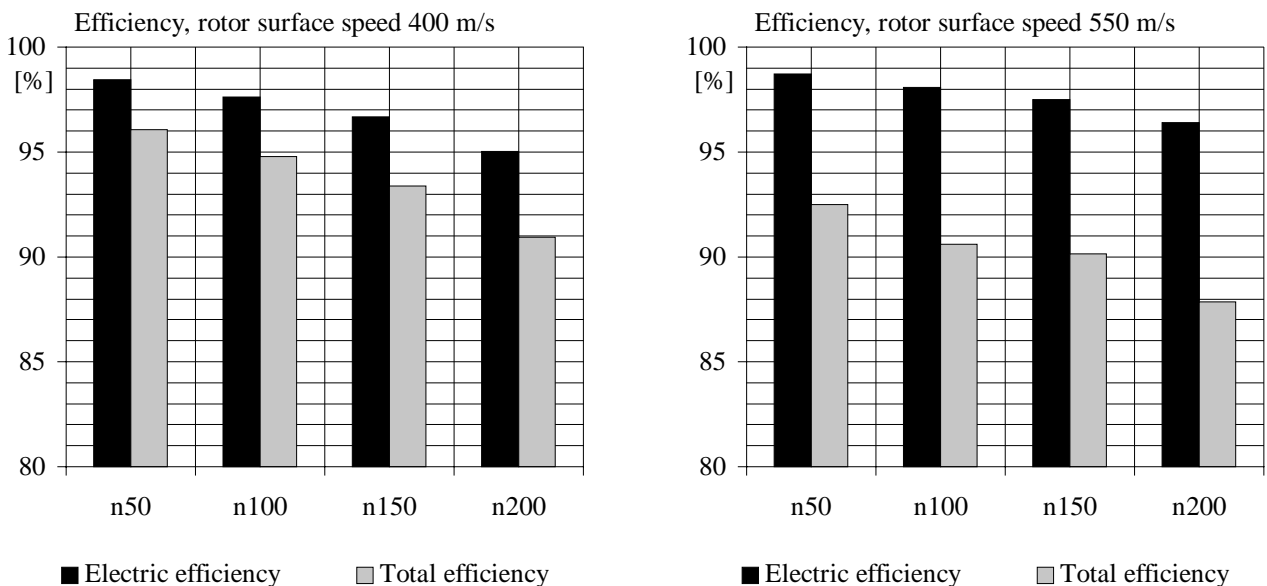


Figure 27. Efficiencies of the motors.

Cooling air flow rate

The powers of the motors are very sensitive to the cooling-duct flow rate. An optimal cooling-duct flow rate for each motor was found as in the case of motor n100v400 (see Fig. 21). The flow rates were between 1.6 and 30.0 m³/min.

The relative share of the gas-flow losses does not vary significantly with the rotation speed if the rotor surface speed is constant. At 400 m/s, the gas-flow losses form about 14% of the total losses. The corresponding figure is 20% at 550 m/s. A constant number means that the total losses are proportional to the cooling-duct flow rate. These figures are about 3 kW/(m³/min) and 4 kW/(m³/min) at rotor surface speeds 400 m/s and 550 m/s, respectively. The efficiency of the cooling increases with the rotor surface speed because of the higher relative share of the friction losses.

In every motor, the temperature of the stator winding limited the power. The rotor never reached 150 K, as the air-gap length was large enough to enable low rotor losses and a high flow rate. On the other hand, large air-gap lengths led to rather low power factors, 0.41-0.74. Larger power factors could be achieved by using smaller air gaps but then the maximum powers would also be lower.

The best efficiency is reached at different cooling-duct flow rates than the highest power. The highest efficiency point moves towards lower air-gap flow rate when the surface speed of the rotor increases. This is due to gas-flow losses, which are proportional to the square of the rotor surface speed and the flow rate. If we take the ventilator power into account the best efficiency moves towards to lower cooling-duct flow rates.

4.5 Discussion

A load machine connected on the shaft decreases the bending critical speeds of the rotor. In order to operate below the first critical speed, the rotor has to be made shorter than given in Table 8. On the other hand, the rotors could also be made longer and run, for instance, between the second and third critical speeds. This would increase the power significantly but it would also put strict demands on the bearings and balancing of the rotors. In these cases, Eq. 33 with the utilisation factors given above can be used for rough estimates of the maximum power.

The motors studied are not fully optimised. Their electromechanical properties could be improved by optimising the dimensions of the stator and by selecting the best materials. The cooling of the larger motors could be improved by using more cooling ducts in the stator core. This would increase the cooling surface and allow higher coolant flow rates. In the present method, the gas is forced to circulate by an overpressure. In this process, the temperature of the inlet gas rises and the cooling capacity decreases. A more efficient way would be to use suction for circulating the gas in which case the inlet gas would be at the room temperature. The cooling solutions of these motors are close to the ones used in large turbogenerators. In both machines, the use of hydrogen or helium

gives higher powers and efficiencies than air cooling. The complicated helium or hydrogen cooling systems may not, however, be very cost effective in high-speed motors.

Even with the improvements discussed above, the powers predicted for the solid-rotor induction motor are considerably higher than the powers found from literature for the existing high-speed machines. Figure 25 shows a 5-15 fold increase in power. The constructions and the method of analysis have not been verified in the extreme conditions (surface speed 550 m/s) required for the maximum powers but they have been applied with good results to motors with surface speeds close to 400 m/s (see Chapter 3). Thus, it is believed that the motor construction presented significantly expands the power range of high-speed motors.

5 CONCLUSIONS

The thesis concentrates on the thermal analysis of high-speed induction machines. The friction and gas-flow losses have been studied in detail. A thermal-network model for a new high-speed induction machine construction has been developed. By using the thermal model, the maximum power of the new motor construction at several rotation speed has been evaluated.

Friction losses caused by the rotor rotation form a significant part of the total losses in high-speed electric machines. These losses can be predicted by analytical equations. Surface roughness caused by the stator slot openings affects very little the friction losses in the air gap, and equations assuming smooth air-gap surfaces can be used. The total friction losses calculated agreed well with the measurements in the two high-speed motors tested.

High-speed induction machines need a coolant flow through the air gap because of their high friction losses. Some power is needed to accelerate the coolant flow into a tangential movement in the air gap. This gas-flow loss can be calculated by an analytical equation. In a smooth rotor and slotted stator surfaces, the gas-flow loss is only about 30% of the figure that can be predicted based on literature for smooth air-gap surfaces.

A thermal-network model for the high-speed induction machines has been developed. The model is valid at different rotation speeds and cooling conditions. This results from the implementation of the friction and gas-flow losses as well as the convection heat-transfer coefficients into the model. The calculated temperature rises of the stator winding were within $\pm 10^{\circ}\text{C}$ the measured ones in the two high-speed motors tested. The test motors have ratings 235 kW, 32 100 rpm and 65 kW, 100 000 rpm. The proper modelling of the heating of the coolant flow is very important as its temperature raises typically by 60-80 K while flowing through the machine.

The maximum power of the new high-speed induction motor construction was evaluated. For this reason, eight motors rotating at speeds 50 000, 100 000, 150 000 and 200 000 rpm were analysed by the thermal-network model. At each rotation speed, the rotor volume was first maximised. The rotor diameter was limited by the strength of the rotor and the rotor length by the first critical bending speed. The maximum powers obtained decrease with the rotation speed to the power of 2.1-2.2. For every motor, the maximum power was obtained at same slip which gave the highest electric efficiency of the machine. The power depends greatly on the air-gap flow. The utilisation factor and the efficiency of the motor decrease when the rotor surface speed increases.

REFERENCES

- Arkkio A. 1987. *Analysis of induction motors based on the numerical solution of the magnetic field and circuit equations*. Acta Polytechnica Scandinavia, Electrical Engineering Series No. 59. Helsinki, Finland, 97 p.
- Becker K.M. and Kaye J. 1962. *Measurements of diabatic flow in an annulus with an inner rotating cylinder*. Transactions of the ASME, Journal of Heat Transfer, Vol. 84, May, pp. 97–105.
- Bilgen E. and Boulos R. 1973. *Functional dependence of torque coefficient of coaxial cylinders on gap width and Reynolds numbers*. Transactions of ASME, Journal of Fluids Engineering, Series I, Vol. 95, No. 1, pp. 122–126.
- Carew N.J. and Freeston D.H. 1967. *Fluid flow losses in a.c. generator stator ventilating ducts*. Institution of Mechanical Engineers, Proceedings 1967-1968, Vol. 182, Part 3D, pp. 87-95.
- Daily J.W. and Nece R.E. 1960. *Chamber dimension effects on induced flow and frictional resistance of enclosed rotating disks*. Transactions of the ASME, Journal of Basic Engineering, Vol. 82, No. 1, March, pp. 217–232.
- Di Prima R.C. and Swinney H.L. 1981. *Instabilities and transition in flow between concentric rotating cylinders*. Hydrodynamic Instabilities and the Transition to Turbulence, Topics in Applied Physics, Editors: Swinney H.L. and Gollub J.P., Vol. 45, Springer-Verlag, Germany, pp. 139–180.
- Dorfman L.A. 1963. *Hydrodynamic resistance and the heat loss of rotating solids*. Oliver & Boyd, Edinburgh and London, 244 p.
- Gazley C. Jr. 1958. *Heat transfer characteristics of the rotational and axial flow between concentric cylinders*. Transactions of the ASME, Vol. 80, pp. 79–90.
- Jokinen T. and Saari J. 1997. *Modelling of the coolant flow with heat flow controlled temperature sources in thermal networks*. IEE Proceedings of Electric Power Appl., Vol. 144, No. 5, pp. 338–342.
- Kreith F. 1968. *Convection heat transfer in rotating systems*. Advances in Heat Transfer, Vol. 5, Academic Press, Inc, USA, pp. 129–251.

- Kylander G. 1995. *Thermal modelling of small cage induction motors*. Technical report No. 265. Chalmers University of Technology, Göteborg, Sweden, 113 p.
- Lantto E. 1997. *Finite-element model for elastic rotating shaft*. Acta Polytechnica Scandinavica, Electrical Engineering Series, No. 88. Espoo, Finland, 73 p.
- Larjola J., Sallinen P., Lindgren O., Esa H., Pyrhönen J., Lattu J. and Falck R. 1991a. *Basic research in high-speed technology*. (in Finnish). Lappeenranta University of Technology, Research report EN B-71, Finland, 185 p.
- Larjola J., Lindgren O. and Vakkilainen E. 1991b. *Utilisation of the industrial and marine waste heat by converting it into electric power with a new technology ORC-plant*. (in Finnish). Ministry of Trade and Industry, MTI Series D:194, Finland, 125 p.
- Lathrop D.P., Fineberg J. and Swinney H.L. 1992a. *Turbulent flow between concentric rotating cylinders at large Reynolds number*. Physical Review Letters, Vol. 68, No. 10, pp. 1515–1518.
- Lathrop D.P., Fineberg J. and Swinney H.L. 1992b. *Transition to shear-driven turbulence in Couette-flow*. Physical Review A, Vol. 46, No. 10, pp. 6390–6405.
- Mellor P.H., Roberts D. and Turner D.R. 1991. *Lumped parameter thermal model for electrical machines of TEFC design*. IEE Proceedings-B, Vol. 138, No. 5, April, pp. 205-218.
- Panton R.L. 1992. *Scaling laws for the angular momentum of the completely turbulent Couette flow*. Comptes Rendus de l'Academie des Sciences. Vol. 315, Serie II, No. 12, pp. 1467–1473.
- Patent U.S. 5473211. *Asynchronous electric machine and rotor and stator for use in association therewith*. High Speed Tech Oy Ltd, Tampere, Finland, Appl. No. 86880, 7.7.1992, 9 p.
- Peesel H. 1958. *Über das Verhalten eines Asynchronmotors bei verschiedenen Läufern aus massivem Stahl*. Doctoral Thesis, Technical University of Braunschweig, 57 p.
- Perez I.J. and Kassakian J.G. 1979. *A stationary thermal model for smooth air-gap rotating electric machines*. Electric Machines and Electromechanics, No. 3–4, pp. 285–303.
- Pickering S.J., Lampard D., Hay N. and Roylance T.F. 1995. *Heat-transfer from the stator end-winding of a low voltage concentric-wound induction motor*. Electrical Machines and Drives, 11-13 September 1995, IEE Conference Publication No. 412, pp. 477-481.

Polkowski J.W. 1984. *Turbulent flow between coaxial cylinders with the inner cylinder rotating*. Transactions of the ASME, Journal of Engineering for Gas Turbines and Power. Vol. 106, No. 1, pp. 128–135.

Rao K.V.C. 1979. *Heat transfer in an annulus with a rotating rough inner cylinder*. Doctoral Thesis, Indian institute of Technology, Department of Mechanical Engineering, Heat Transfer and Thermal Power Laboratory, Madras, India, 210 p.

Reynolds A.J. 1974. *Turbulent flows in engineering*. John Wiley & Sons Ltd., 462 p.

Saari J. 1996. *Friction losses and heat transfer in high-speed electrical machines*. A literature review, Helsinki University of Technology, Laboratory of Electromechanics, Report 50, Espoo, Finland, 34 p.

Saari J. 1995. *Thermal modelling of high-speed induction machines*. Acta Polytechnica Scandinavica, Electrical Engineering Series No. 82. Helsinki, Finland, 82 p.

Smith G.P. and Townsend A.A. 1982. *Turbulent Couette flow between concentric cylinders at large Taylor numbers*, Journal of Fluid mechanics, Vol. 123, pp. 187–217.

Theodorsen T. and Regier A. 1944. *Experiments of drag of revolving disks, cylinders, and streamline rods at high speeds*. Thirtieth annual report of the National Advisory Committee for Aeronautics (NACA), Technical Report No. 793, pp. 367–384.

Ueyama H. and Fujimoto Y. 1990. *Iron losses and windy losses of high rotational speed rotor suspended by magnetic bearings*. Second International Symposium on Magnetic Bearing, July 12–14, Tokyo, Japan, pp. 237–242.

Wendt F. 1933. *Turbulente Strömungen zwischen zwei rotierenden konaxialen Zylindern*. Ingenieur-Archiv, Vol. 9, pp. 577–595.

Vogt K. 1983. *Elektrische Maschinen, Berechnung rotierender elektrischer Maschinen*. 3. bearbeitete Auflage, VEB Verlag Technik, Berlin, GDR, 500 p.

Yamada Y. 1962a. *Torque resistance of a flow between rotating co-axial cylinders having axial flow*. Bulletin of JSME, Vol. 5, No. 20, pp. 634–642.

Yamada Y. 1962b. *Resistance of a flow through an annulus with an inner rotating cylinder*. Bulletin of JSME, Vol. 5, No. 18, pp. 302–310.

APPENDIX A: THERMAL NETWORK FOR HIGH-SPEED INDUCTION MACHINES

Figure A1 presents the thermal network for the high-speed induction machines. The calculation of the thermal resistance components is presented by Eqs. A1–A58. The symbols used in the equations are described in Fig. A2 and Table A1.

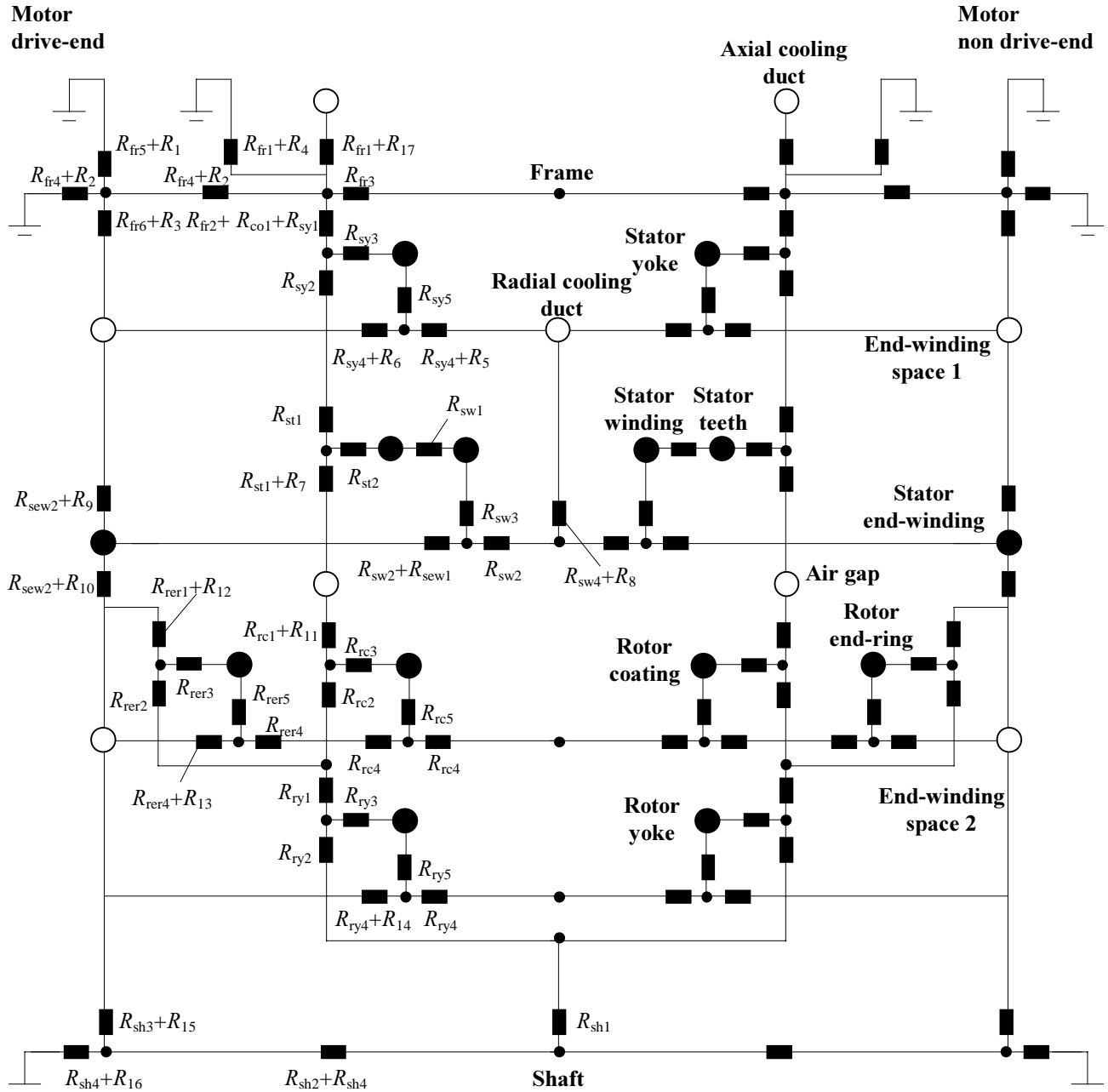


Figure A1. Circuit diagram of the thermal model for high-speed induction machines. Open circles refer to node points located in air space of the machine (cooling ducts, air gap etc.). The electric heat generation appears in the node points marked with big black circles (stator yoke, rotor coating etc.).

Thermal resistances in frame

$$R_{fr1} = \frac{\ln\left(\frac{2r_{fr2}}{2r_{fr1} + h_{fr}}\right)}{2\pi l_{fr1} k_{fr}} \quad (A1)$$

$$R_{fr2} = \frac{\ln\left(\frac{2r_{fr1} + h_{fr}}{2r_{fr1}}\right)}{2\pi l_{fr1} k_{fr}} \quad (A2)$$

$$R_{fr3} = \frac{l_{fr1}}{2\pi(r_{fr2}^2 - r_{fr1}^2)k_{fr}} \quad (A3)$$

$$R_{fr4} = \frac{l_{fr2}}{2\pi(r_{fr2}^2 - r_{fr1}^2)k_{fr}} \quad (A4)$$

$$R_{fr5} = \frac{\ln\left(\frac{2r_{fr2}}{2r_{fr1} + h_{fr}}\right)}{2\pi l_{fr2} k_{fr}} \quad (A5)$$

$$R_{fr6} = \frac{\ln\left(\frac{2r_{fr1} + h_{fr}}{2r_{fr1}}\right)}{2\pi l_{fr2} k_{fr}} \quad (A6)$$

Thermal resistances in stator core

$$R_{co1} = \frac{1}{2\pi r_{fr1} l_{fr1} k_{co1}} \quad (A7)$$

$$R_{sy1} = \frac{1}{4\pi l_{sc} k_{scr}} \left[1 - \frac{2r_{s2}^2 \ln\left(\frac{r_{fr1}}{r_{s2}}\right)}{r_{fr1}^2 - r_{s2}^2} \right] \quad (A8)$$

$$R_{sy2} = \frac{1}{4\pi l_{sc} k_{scr}} \left[\frac{2r_{fr1}^2 \ln\left(\frac{r_{fr1}}{r_{s2}}\right)}{r_{fr1}^2 - r_{s2}^2} - 1 \right] \quad (A9)$$

$$R_{sy3} = \frac{-1}{8\pi(r_{fr1}^2 - r_{s2}^2)l_{sc}k_{scr}} \left[r_{fr1}^2 + r_{s2}^2 - \frac{4r_{fr1}^2 r_{s2}^2 \ln\left(\frac{r_{fr1}}{r_{s2}}\right)}{r_{fr1}^2 - r_{s2}^2} \right] \quad (A10)$$

$$R_{sy4} = \frac{l_{sc}}{2\pi(r_{fr1}^2 - r_{s2}^2)l_{sc}k_{sca}} \quad (A11)$$

$$R_{sy5} = \frac{-1}{3R_{sy4}} \quad (A12)$$

$$R_{st1} = \frac{h_{ss}}{2\left[\pi(2r_{s1} + h_{ss}) - N_s b_{ss2}\right]l_{sc}k_{scr}} \quad (A13)$$

$$R_{st2} = \frac{-1}{3R_{st1}} \quad (A14)$$

Thermal resistances in stator winding

$$R_{sw1} = \frac{1}{l_{sc}N_s} \left(\frac{1}{4\pi k_{swr}} + \frac{b_{ssi}}{(2h_{ss} + b_{ss2})k_{ssi}} + \frac{1}{(2h_{ss} + b_{ss2})h_{co2}} \right) \quad (A15)$$

$$G_w = \frac{1}{R_{sw1}} \quad (A16)$$

$$R_w = \frac{l_{sc}}{N_s k_f A_{ss} k_{swa}} \quad (A17)$$

$$R_{sw2} = \sqrt{\frac{R_w}{G_w}} \tanh \sqrt{\frac{R_w G_w}{2}} \quad (A18)$$

$$R_{sw3} = \frac{1}{G_w} \left(\frac{\sqrt{R_w G_w}}{\sinh \sqrt{\frac{R_w G_w}{2}}} - 1 \right) \quad (A19)$$

$$R_{sw4} = \frac{1}{l_{cd}N_s} \left(\frac{1}{4\pi k_{swr}} + \frac{b_{ssi}}{(2h_{ss} + b_{ss2})k_{ssi}} + \frac{1}{(2h_{ss} + b_{ss2})h_{co3}} \right) \quad (A20)$$

$$R_{\text{sew1}} = \frac{3}{2} \frac{l_{\text{sew}}}{N_s k_f A_{\text{ss}} k_{\text{swa}}} \quad (\text{A21})$$

$$R_{\text{sew2}} = \frac{3}{2} \frac{1}{4\pi^2 (r_{\text{sew1}} + r_{\text{sew2}}) k_{\text{swr}}} \quad (\text{A22})$$

Thermal resistances in rotor core

$$R_{\text{ry1}} = \frac{1}{4\pi(l_{\text{rc}} + l_{\text{rer}})k_{\text{rcr}}} \left[1 - \frac{2r_{\text{sh}}^2 \ln\left(\frac{r_{\text{r1}}}{r_{\text{sh}}}\right)}{r_{\text{r1}}^2 - r_{\text{sh}}^2} \right] \quad (\text{A23})$$

$$R_{\text{ry2}} = \frac{1}{4\pi(l_{\text{rc}} + l_{\text{rer}})k_{\text{rcr}}} \left[\frac{2r_{\text{sh}}^2 \ln\left(\frac{r_{\text{r1}}}{r_{\text{sh}}}\right)}{r_{\text{r1}}^2 - r_{\text{sh}}^2} - 1 \right] \quad (\text{A24})$$

$$R_{\text{ry3}} = \frac{-1}{8\pi(r_{\text{r1}}^2 - r_{\text{sh}}^2)(l_{\text{rc}} + l_{\text{rer}})k_{\text{kcr}}} \left[r_{\text{r1}}^2 + r_{\text{sh}}^2 - \frac{4r_{\text{r1}}^2 r_{\text{sh}}^2 \ln\left(\frac{r_{\text{r1}}}{r_{\text{sh}}}\right)}{r_{\text{r1}}^2 - r_{\text{sh}}^2} \right] \quad (\text{A25})$$

$$R_{\text{ry4}} = \frac{l_{\text{rc}} + l_{\text{rer}}}{2\pi(r_{\text{r1}}^2 - r_{\text{sh}}^2)k_{\text{rca}}} \quad (\text{A26})$$

$$R_{\text{ry5}} = \frac{-1}{3R_{\text{ry4}}} \quad (\text{A27})$$

Thermal resistances in rotor coating

$$R_{\text{rc1}} = \frac{1}{4\pi l_{\text{rc}} k_{\text{rc}}} \left[1 - \frac{2r_{\text{r1}}^2 \ln\left(\frac{r_{\text{r2}}}{r_{\text{r1}}}\right)}{r_{\text{r2}}^2 - r_{\text{r1}}^2} \right] \quad (\text{A28})$$

$$R_{rc2} = \frac{1}{4\pi l_{rc} k_{rc}} \left[\frac{2r_{r1}^2 \ln\left(\frac{r_{r2}}{r_{r1}}\right)}{r_{r2}^2 - r_{r1}^2} - 1 \right] \quad (A29)$$

$$R_{rc3} = \frac{-1}{8\pi(r_{r2}^2 - r_{r1}^2)l_{rc} k_{rc}} \left[r_{r2}^2 + r_{r1}^2 - \frac{4r_{r2}^2 r_{r1}^2 \ln\left(\frac{r_{r2}}{r_{r1}}\right)}{r_{r2}^2 - r_{r1}^2} \right] \quad (A30)$$

$$R_{rc4} = \frac{l_{rc}}{2\pi(r_{r2}^2 - r_{r1}^2)k_{rc}} \quad (A31)$$

$$R_{rc5} = \frac{-1}{3R_{rc4}} \quad (A32)$$

Thermal resistances in rotor end ring

$$R_{rer1} = \frac{1}{4\pi l_{rer} k_{rc}} \left[1 - \frac{2r_{r1}^2 \ln\left(\frac{r_{rer}}{r_{r1}}\right)}{r_{rer}^2 - r_{r1}^2} \right] \quad (A33)$$

$$R_{rer2} = \frac{1}{4\pi l_{rer} k_{rc}} \left[\frac{2r_{r1}^2 \ln\left(\frac{r_{rer}}{r_{r1}}\right)}{r_{rer}^2 - r_{r1}^2} - 1 \right] \quad (A34)$$

$$R_{rer3} = \frac{-1}{8\pi(r_{rer}^2 - r_{r1}^2)l_{rer} k_{rc}} \left[r_{rer}^2 + r_{r1}^2 - \frac{4r_{rer}^2 r_{r1}^2 \ln\left(\frac{r_{rer}}{r_{r1}}\right)}{r_{rer}^2 - r_{r1}^2} \right] \quad (A35)$$

$$R_{rer4} = \frac{l_{rer}}{2\pi(r_{rer}^2 - r_{r1}^2)k_{rc}} \quad (A36)$$

$$R_{rer5} = \frac{-1}{3R_{rer4}} \quad (A37)$$

Thermal resistances in shaft

$$R_{sh1} = \frac{1}{4\pi r_{sh}(l_{rc} + l_{rer})k_{rc}} \quad (A38)$$

$$R_{sh2} = \frac{l_{rc} + l_{rer}}{\pi r_{sh}^2 k_{rc}} \quad (A39)$$

$$R_{sh3} = \frac{1}{2\pi l_{sh} k_{rc}} \quad (A40)$$

$$R_{sh4} = \frac{l_{sh}}{2\pi r_{sh}^2 k_{rc}} \quad (A41)$$

Convection thermal resistances

$$R_1 = \frac{1}{h_1 \pi (r_{fr2}^2 - r_{fr1}^2)} \quad (A42)$$

$$R_2 = \frac{1}{h_2 2\pi r_{fr2} l_{fr2}} \quad (A43)$$

$$R_3 = \frac{1}{h_3 2\pi r_{fr1} l_{fr2}} \quad (A44)$$

$$R_4 = \frac{1}{h_4 2\pi r_{fr1} l_{fr1}} \quad (A45)$$

$$R_5 = \frac{1}{h_5 [\pi (r_{fr1}^2 - r_{s1}^2) - N_s A_{ss}]} \quad (A46)$$

$$R_6 = \frac{1}{h_6 [\pi (r_{fr1}^2 - r_{s1}^2) - N_s A_{ss}]} \quad (A47)$$

$$R_7 = \frac{1}{h_7 (2\pi r_{s1} - N_s b_{ss1}) l_{sc}} \quad (A48)$$

$$R_8 = \frac{1}{h_8(2h_{ss} + b_{ss1})N_s l_{cd}} \quad (\text{A49})$$

$$R_9 = \frac{1}{h_9 \pi^2 r_{sew} (r_{sew2} + r_{sew1})} \quad (\text{A50})$$

$$R_{10} = \frac{1}{h_{10} \pi^2 r_{sew} (r_{sew2} + r_{sew1})} \quad (\text{A51})$$

$$R_{11} = \frac{1}{h_{11} 2\pi r_{r2} l_{rc}} \quad (\text{A52})$$

$$R_{12} = \frac{1}{h_{12} 2\pi r_{rer} l_{rer}} \quad (\text{A53})$$

$$R_{13} = \frac{1}{h_{13} \pi (r_{rer}^2 - r_{r1}^2)} \quad (\text{A54})$$

$$R_{14} = \frac{1}{h_{14} \pi (r_{r1}^2 - r_{sh}^2)} \quad (\text{A55})$$

$$R_{15} = \frac{1}{h_{15} 2\pi r_{sh} l_{sh}} \quad (\text{A56})$$

$$R_{16} = \frac{1}{h_{16} \pi r_{sh}^2} \quad (\text{A57})$$

$$R_{17} = \frac{1}{h_{17} A_{cd}} \quad (\text{A58})$$

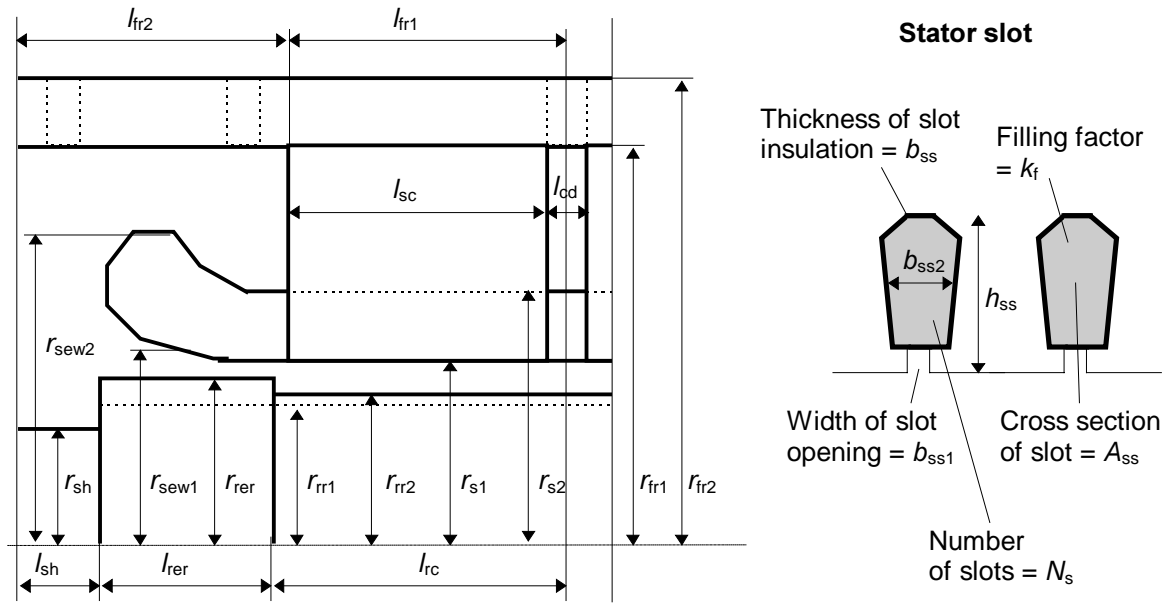


Figure A2. Symbols for the dimensions of the electric motor.

Table A1. Symbols for thermal conductivities, convection heat-transfer coefficients and contact heat-transfer coefficients.

Thermal conductivities	
k_{fr}	Frame
k_{scr}	Stator core; radial direction
k_{sca}	Stator core; axial direction
k_{swr}	Stator winding; radial direction in the stator slot
k_{swa}	Stator winding; along the conductors
k_{ssi}	Insulation in the stator slot
k_{rcr}	Rotor core
k_{rc}	Rotor coating and end ring
k_{sh}	Shaft
Convection heat-transfer coefficients	
h_1	Between frame and ambient air (axial direction)
h_2	Between frame and ambient air (radial direction)
h_3	Between frame and end-winding space (radial direction)
h_4	Between frame and ambient air (radial direction)
h_5	Between stator core and radial cooling duct (axial direction)
h_6	Between stator core and end-winding space (axial direction)
h_7	Between stator teeth and air-gap flow (radial direction)
h_8	Between stator winding and radial cooling duct (radial direction)
h_9	Between stator end-winding (outer surface) and end-winding space
h_{10}	Between stator end-winding (inner surface) and end-winding space
h_{11}	Between rotor coating and air-gap flow (radial direction)
h_{12}	Between rotor end ring and end-winding space (radial direction)
h_{13}	Between rotor end ring and end-winding space (axial direction)
h_{14}	Between rotor core and end-winding space (axial direction)
h_{15}	Between shaft and end-winding space (radial direction)
h_{16}	Between shaft and ambient air (axial direction)
h_{17}	Between frame and axial cooling duct
Contact heat-transfer coefficients	
h_{co1}	Between stator core and frame
h_{co2}	Between stator winding and core (core region)
h_{co3}	Between stator winding and slot insulation (cooling-duct region)

APPENDIX B: REFERRED HIGH-SPEED INDUCTION MACHINES IN FIGURE 17

n [rpm]	P [kW]	Reference
42 000	75	Antila M., Lantto E., Saari J., Esa H., Lindgren O. and Säily K. 1996. <i>Design of water treatment compressors equipped with active magnetic bearings</i> . Proceedings of the Fifth International Symposium on Magnetic Bearings, August 1996, Kanazawa, Japan, pp. 389–394.
50 000	36	Saari J. 1995. <i>Thermal modelling of high-speed induction machines</i> . Acta Polytechnica Scandinavica, Electrical Engineering Series 82, Helsinki, 82 p.
100 000	60	Saari J. and Arkkio A. 1994. <i>Losses in high-speed asynchronous motors</i> . Proceedings of the International Conference on Electrical Machines, 1994, Paris, Vol. 3, pp. 704–708.
14 000	700	Botte R., Boutriau L., Edebouw J.M. and Gilon D. 1992. <i>Douze ans d'experience dans les moteurs asynchrones de grande puissance a tres haute vitesse variable</i> . Revue Generale de l'Electricite, Vol. 11, pp. 28–32.
16 000	1 200	Botte R., Boutriau L., Edebouw J.M. and Gilon D. 1992. <i>Douze ans d'experience dans les moteurs asynchrones de grande puissance a tres haute vitesse variable</i> . Revue Generale de l'Electricite, Vol. 11, pp. 28–32.
10 000	6 000	Botte R., Boutriau L., Edebouw J.M. and Gilon D. 1992. <i>Douze ans d'experience dans les moteurs asynchrones de grande puissance a tres haute vitesse variable</i> . Revue Generale de l'Electricite, Vol. 11, pp. 28–32.
60 000	15	Brunet M. and Wagner B. 1994. <i>Analysis of the performance of an AMB spindle in creep feed grinding</i> . Proceedings of the Fourth International Symposium on Magnetic Bearings, 1994, ETH Zurich, pp. 519–524.
40 000	33	Brunet M. and Wagner B. 1994. <i>Analysis of the performance of an AMB spindle in creep feed grinding</i> . Proceedings of the Fourth International Symposium on Magnetic Bearings, 1994, ETH Zurich, pp. 519–524.
20 000	2 000	Gilon D.C. 1994. <i>Cooling solutions for high-speed high-power induction motors</i> . Proceedings of the International Conference on Electrical Machines, 1994, Paris, Vol. 3, pp. 516–521.
20 000	2 000	Graham A.D. and Wimshurst M. 1993. <i>The high speed oil free intelligent motor-compressor</i> . Proceedings of Fifth European Conference on Power Electronics and Applications. Brighton, IEE Conference Publications 377, Vol. 5, pp. 384–389.
15 600	2 300	Odegard B., Stulz C.A. and Steimer P.K. 1996. <i>High-speed, variable-speed drive system in megawatt power range</i> . IEEE Industry Application Magazine, May/June, pp. 43–50.

n [rpm]	P [kW]	Reference
10 000	6 000	Oliver J.A. and Poteet D. 1995. <i>High-speed, high-horsepower electric motors for pipeline compressors: Available ASD technology, reliability, harmonic control</i> . IEEE Transactions on Energy Conversion, Vol. 10, 3, pp. 470–476.
10 800	6 000	Rama J.C. and Giesecke A. 1995. <i>High speed electric drive applications, experience, potential & pitfalls - a global overview</i> . Proceedings of the Industry Applications Society 42nd Annual Petroleum and Chemical Industry Conference, pp. 16-24.
10 000	3 375	Rama J.C. and Giesecke A. 1995. <i>High speed electric drive applications, experience, potential & pitfalls - a global overview</i> . Proceedings of the Industry Applications, Society 42nd Annual Petroleum and Chemical Industry Conference, pp. 16-24.
30 000	100	Reichert K. and Pasquarella G. 1995. <i>High speed electric machines, status, trends and problems</i> . Proceedings of the Stockholm Power Tech Conference, Stockholm, Sweden, Vol. Invited Speakers' Sessions, pp. 41– 49.
11 160	2 625	Wood B.M., Olsen C.L., Hartzo G.D., Rama J.C. and Szenasi F.R. 1995. <i>Development of an 11000 r/min, 3500 hp induction motor and adjustable speed drive for refinery service</i> . Proceedings of the Industry Applications Society 42nd Annual Petroleum and Chemical Industry Conference, pp. 55-63.
12 000	10	Andresen E. Ch., Pfeiffer R. and Werth L. 1989. <i>Fundamentals for the design of high speed induction motor drives with transistor inverter supply</i> . Proceedings of EPE'89, 9–12 October 1989, Aachen, Germany, Vol. 2, pp. 823–828.
30 000	7.5	Boglietti A., Ferraris P., Lazzari M. and Profumo F. 1990. <i>Test procedure for very high speed spindle motors</i> . Conference Record of the IEEE-IAS Annual meeting, Vol. 1, pp. 102–108.
40 000	40	Colton B. 1990. <i>What it takes to choose a high-speed AC motor</i> . Power Transmission Design, Vol. 9, pp. 45–47.
10 000	560	Colton B. 1990. <i>What it takes to choose a high-speed AC motor</i> . Power Transmission Design, Vol. 9, pp. 45–47.
21 480	8.9	Colton B. 1990. <i>What it takes to choose a high-speed AC motor</i> . Power Transmission Design, Vol. 9, pp. 45–47.
50 570	3.7	Colton B. 1990. <i>What it takes to choose a high-speed AC motor</i> . Power Transmission Design, Vol. 9, pp. 45–47.
20 000	14.9	Colton B. 1990. <i>What it takes to choose a high-speed AC motor</i> . Power Transmission Design, Vol. 9, pp. 45–47.
10 000	6 000	Gilon D. C. 1991. <i>Design and tests of a 6 MW, 10000 rpm induction motor</i> . Fifth International Conference on Electrical Machines and Drives, 11–13 September 1991, London, IEE Conference Publications 341, 1991, pp. 6–10.

n [rpm]	P [kW]	Reference
12 000	200	Ikeda M., Sakabe S. and Higashi K. 1990. <i>Experimental study of high speed induction motor varying rotor core construction</i> . IEEE Transactions on Energy Conversion, Vol. 5, 1, pp. 98–103.
40 000	15	Kume T., Sawa T., Yoshida T., Sawamura M. and Sakamoto M. 1992. <i>A high-speed vector-controlled spindle motor drive with closed transition between with encoder control and without encoder control</i> . IEEE Transactions on Industry Applications, Vol. 28, 2, pp. 421–429.
15 000	32	Meyer R. 1990. <i>Die Projektierung von hochtourigen Antrieben mit Mittelfrequenz Motorelementen</i> . Elektrische Maschinen, 69, 4, pp. 94–105.
90 000	3	Meyer R. 1990. <i>Die Projektierung von hochtourigen Antrieben mit Mittelfrequenz Motorelementen</i> . Elektrische Maschinen, 69, 4, pp. 94–105.
16 400	37	Ohsawa M., Kanemitsu Y., Katsuta S., Kobayashi F., Yoshida K. and Rush S. 1992. <i>High speed submerged motor pump for liquefied natural gas service supported by magnetic bearings</i> . Proceedings of the Third International Symposium on Magnetic Bearings, Alexandria, USA, pp. 401-410.
24 000	12	Pyrhönen J. 1991. <i>Calculating the effects of solid-rotor material on high-speed induction motor characteristics</i> . European Transactions on Electrical Power Engineering, Vol. 1, 6, pp. 301–310.
18 000	3.5	Reisinger E. and Huber A. 1992. <i>Hochtourige Antriebe mit Asynchronmaschinen</i> . Elektrotechnik und informationstechnik, Vol. 109, 6, pp. 307–309.
40 000	30	Waldvogel U.G. 1991. <i>Schnellfrequenz-Motorspindeln mit höheren Drehzahlen und mehr Leistung</i> . Schweizerische Technische Zeitschrift, Vol. 88, 11, pp. 9–13.

APPENDIX C: PERFORMANCE OF THE HIGH-SPEED MOTORS

Motor code		Rotor surface speed 400 m/s				Rotor surface speed 550 m/s			
		n50	n100	n150	n200	n50	n100	n150	n200
Shaft power	[kW]	1048	235	105	50	1390	327	156	76
Torque	[Nm]	197.1	22.6	6.7	2.4	261.4	31.3	10.0	3.6
Supply frequency	[Hz]	850	1670	2500	3350	850	1670	2500	3350
Slip	[%]	0.4	0.7	0.9	0.8	0.4	0.6	0.7	0.75
Rotation speed	[rpm]	50796	99499	148650	199392	50796	99599	148950	199493
Power factor		0.66	0.63	0.54	0.41	0.74	0.68	0.6	0.54
Air-gap flux density	[T]	0.37	0.36	0.39	0.43	0.26	0.28	0.32	0.34
Rotor diameter	[mm]	153.0	76.0	51.0	38.0	210.0	105.0	70.0	52.0
Rotor length	[mm]	673	334	224	167	777	389	259	192
Air-gap length	[mm]	5.5	3.0	2.5	2.0	6.0	4.0	3.0	2.0
Pressure drop	[kPa]	12.13	8.78	10.78	11.05	22.49	15.67	12.66	15.30
Inlet temperature rise	[K]	13.00	9.50	11.60	11.88	23.43	16.63	13.55	16.25
Cool.-duct flow rate	[m ³ /min]	15.0	4.0	2.5	1.6	30.0	9.0	4.0	2.5
End-wind. flow rate	[m ³ /min]	140.0	60.0	30.0	18.0	160.0	60.0	60.0	18.0
Stator losses	[kW]	8.04	3.00	1.96	1.50	7.56	3.51	2.32	1.57
Rotor losses	[kW]	8.80	2.93	1.78	1.21	11.83	3.42	2.01	1.53
Friction losses	[kW]	19.72	5.37	2.67	1.59	69.35	19.95	9.64	5.48
Gas-flow losses	[kW]	6.39	1.61	1.01	0.65	24.10	6.94	3.07	1.90
Ventilator power	[kW]	34.83	10.51	6.52	4.03	77.05	19.84	14.99	5.76
Electric efficiency	[%]	98.46	97.61	96.67	95.03	98.71	98.08	97.50	96.42
Total efficiency	[%]	96.06	94.80	93.39	90.94	92.49	90.62	90.17	87.87
Utilisation factor	[Nm/dm ³]	15.9	14.9	14.7	12.6	9.7	9.3	10.1	8.7
Stator temp. rise	[K]	104.7	104.8	104.8	102.3	101.9	104.7	104.6	102.9
Rotor temp. rise	[K]	142.8	134.6	143.8	152.6	153.1	132.8	137.2	152.9